Acta Mech
https://doi.org/10.1007/s00707-026-04765-8

ORIGINAL PAPER

Alim Berk Çağlayan · Büşra Uzun

On axial dynamic analysis of viscoelastic nanorods reinforced with particles

Received: 13 March 2026 / Revised: 12 May 2026 / Accepted: 18 May 2026
© The Author(s) 2026

Abstract This study proposes an analytical model for the size-dependent axial vibration of particle-reinforced viscoelastic nanorods. Size effects and viscoelastic damping are incorporated utilizing nonlocal elasticity theory and the Kelvin–Voigt model, respectively, while the effective mechanical properties are determined via the Mori–Tanaka homogenization scheme. A key novelty of this work is the analytical formulation and solution of characteristic equations for a broad range of boundary conditions, evolving in a generalized configuration where a lumped mass and an elastic spring are simultaneously present at the rod's extremity. The study systematically investigates the influence of particle volume fraction, nonlocal size effects, material damping, and boundary mass-spring parameters. It is found that the particle reinforcement ratio, nonlocal scale dependency, and the inertial dominance of the attached mass play pivotal roles in modulating the axial vibration and attenuation performance of the nanorods. Ultimately, this comprehensive theoretical framework provides critical insights for the design and optimization of advanced nano-electro-mechanical systems (NEMS) and nanoresonators.

1 Introduction

The trajectory of technological progress has evolved from gaining the capacity for nanoscale observation in the twentieth century to achieving nanometer-level manipulation and manufacturing in the twenty-first century. Recent breakthroughs in nanotechnology have facilitated the design of next-generation engineering materials that exhibit superior mechanical properties alongside unique electrical and thermal performances. Gaining significant momentum following Iijima's [1] synthesis of carbon nanotubes (CNTs), this era has witnessed the development of nano-electro-mechanical systems (NEMS) utilizing structural elements such as nanorods, nanowires, nanobeams, and nanoplates. These NEMS serve as fundamental building blocks in high-precision biomedical devices [2–4], sensor architectures with precise actuation mechanisms [5–7], energy-harvesting units [8, 9], and high-capacity processors [10, 11]. In such systems, which are expected to deliver both adequate mechanical performance and specific functional capabilities, traditional materials are increasingly being superseded by advanced materials that possess superior engineering characteristics and the potential to satisfy multi-functional requirements. Although functionally graded materials (FGMs) have gained prominence in this context, the narrowing processing tolerances associated with dimensional scaling present significant challenges for fabricating such structures at the nanoscale given current manufacturing limitations. Consequently, the utilization of reinforced composite structures has emerged as a viable alternative. Formed by combining at least two distinct materials, reinforced composites aim to synergistically exploit the superior properties of their constituent components. For instance, while one constituent may offer exceptional

A. B. Çağlayan · B. Uzun (✉)
Department of Civil Engineering, Engineering Faculty, Bursa Uludag University, Görükle, Campus, 16059 Bursa, Turkey
e-mail: buzun@uludag.edu.tr

A. B. Çağlayan
e-mail: acaglayan@uludag.edu.tr

Published online: 15 June 2026

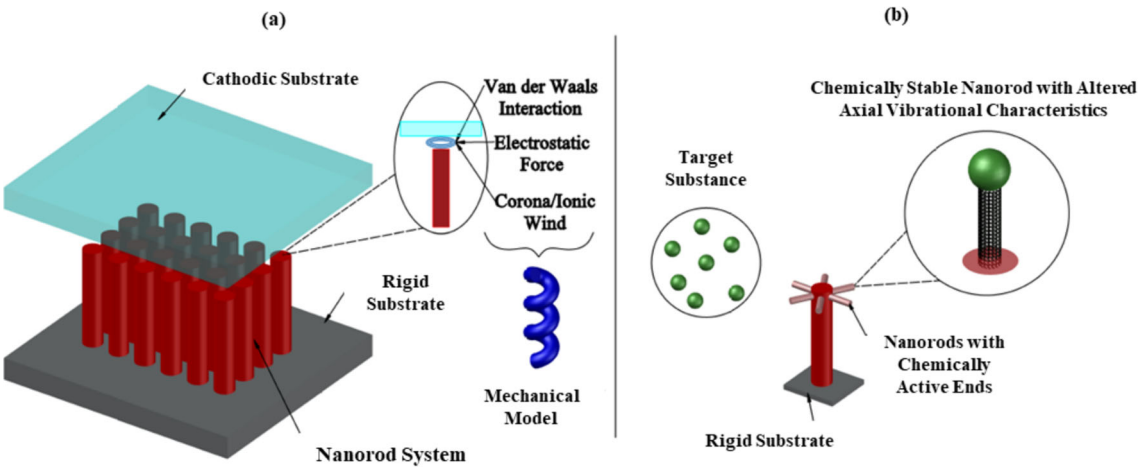


Fig. 1 **a** Force-driven nanorod system. **b** Material composition detection using a nanomechanical mass sensor

mechanical strength, another may provide chemical stability or enhance electrical conductivity. Consequently, understanding the response of these performance-oriented composite structures to mechanical effects at the nanoscale mandates a theoretical framework that goes beyond classical elasticity approaches, which typically disregard small-scale effects.

When evaluating the mechanical behavior of micro- or nanoscale structures, phenomena such as interatomic interactions and intermolecular bonding forces become highly significant. Classical continuum mechanics inherently excludes these microscopic interactions and size effects from its formulations. Consequently, as structural dimensions' shrink, classical approaches fall short in accurately modeling the true physical reality. To mathematically capture this scale dependency, various size-dependent frameworks have been proposed in the literature, including strain gradient theory [12, 13], modified couple stress theory [14], surface effect formulations [15, 16], and peridynamics [17, 18]. As is readily apparent from the literature, these size-dependent theories have frequently been utilized to describe the mechanical responses of a wide spectrum of small-scale elements. Such applications range from one-dimensional structures like functionally graded (FG) porous microbeams/nanobeams [19, 20], CNT-reinforced micro-/nanobeams [21, 22], dielectric elastomer microresonators [23], and axially loaded nanobeams with deformable boundaries [24], to more complex two-dimensional architectures. These advanced 2D and 3D configurations encompass smart piezomagnetic sandwich nanosensor plates [25, 26], auxetic and active FGM sandwich nanoplates [27, 28], and even porous FG/lipid bionanoplates [29].

Among these methodologies, the nonlocal elasticity theory (NET) proposed by Eringen [30, 31] stands out as the most widely adopted framework, primarily due to its computational efficiency and physical consistency in the static and dynamic analysis of nanostructures. The core postulate of this theory deviates from the local assumption, which restricts the stress at a reference point solely to the strain at that exact location, by defining stress as a functional of the strain field across all points in the continuum. The nonlocal parameter, integrated into classical constitutive relations and calibrated via atomic models, introduces a softening effect by embedding the influence of long-range interatomic forces into the continuum model. A substantial portion of the existing literature focusing on the mechanics of various nanoscale structures such as purely elastic FG nanobeams [32, 33], nanoplates [34, 35], and composite nanoshells [36, 37] leverages NET to account for size-dependent phenomena.

One-dimensional nanostructures, especially nanorods, play a pivotal role in modern engineering applications. Thanks to their exceptional electromechanical properties and high surface-to-volume ratios, nanorods are extensively utilized as fundamental components in NEMS, nanoscale circuits [38], highly efficient electrodes [39], and ultra-sensitive mass and force sensors [40, 41]. In the operational and mathematical modeling of these advanced devices, nanorods frequently interact with external elements. For instance, in resonant-based mass sensing applications, target biological or chemical molecules binding to the nanostructure are typically modeled as attached discrete masses [42]. Similarly, the interactions of a nanorod with an end contacting elastic medium, polymer matrix, or adjacent micro-/nanocomponents are mathematically idealized using attached elastic springs. To serve as an example of rod-mass-spring systems modeled in the nanoenvironment, representative schematic illustrations are presented in Fig. 1 [43–45].

The size-dependent dynamic responses of nanorods have been reported in various studies, particularly based on NET. For instance, Aydoğdu [46, 47] investigated the axial vibration of nanorods under various boundary conditions using this theory. Focusing on geometric discontinuities, Nassef [48] and Taima et al. [49] analyzed the dynamic responses of cracked nanorods with variable cross sections and stepped nanorods, respectively, elucidating the frequency shifts induced by structural irregularities in nonlocal systems. From a material composition perspective, Nazemnezhad [50], Uzun et al. [51], and Uzun [52] investigated axially FG materials, FG porous structures, and short-fiber-reinforced composites, respectively, evaluating the axial vibration characteristics of nanorods composed of these materials within a nonlocal framework. Arda et al. [53] investigated wave propagation in axially FG Rayleigh–Bishop nanorods through the lens of nonlocal elasticity. Concentrating on boundary conditions, Xu et al. [54] analyzed the impact of internal elastic supports on axial vibration in conjunction with NET. Yazıcıoğlu and Civalek [55] studied the axial and torsional vibrations of boron nitride nanotubes, incorporating size effects into their model using nonlocal elasticity theory. Numanoğlu et al. [56] addressed the axial vibration behavior of nanorods with mass or spring attachments within the framework of nonlocal elasticity theory.

Despite the breadth of these investigations, most rely on the assumption of linear elasticity. This presents a critical gap, as materials in real-world engineering contexts inevitably display viscoelastic damping behaviors, driving internal friction and consequent energy dissipation. Accounting for viscoelastic material behavior in the dynamic analysis of nanostructures is crucial for embedding a physically realistic material norm within the mathematical model. To simulate material damping, the literature predominantly relies on the Kelvin–Voigt model, which consists of an elastic spring paired in parallel with a viscous dashpot, configuration that mathematically dictates an iso-strain condition [57]. Investigations reveal that introducing this viscoelastic assumption transforms the vibration frequencies of dynamic systems into complex quantities. Crucially, the viscoelastic damping mechanism is noted to exert a profound impact, particularly in modulating vibration amplitudes at higher modes.

This paradigm has driven extensive research across various structural and material configurations. Exploring wave dynamics, Rahmani et al. [58] modeled rotating viscoelastic nanobeams, capturing scale effects by fusing the modified couple stress theory with NET. In a related vein, Alrubea and Abouelregal [59] probed the thermoelastic responses of viscoelastic nanobeams, deploying the Kelvin–Voigt model to account for both temporal and spatial nonlocality. Shifting the focus to material heterogeneity, Balci [60] analyzed the forced vibration of a radially FG porous viscoelastic nanorod, integrating size effects via NET. The critical role of boundary conditions was highlighted by Kadıoğlu and Yaylı [61], who assessed the nonlocality-driven axial vibration of FG viscoelastic nanorods supported by deformable constraints. In a similar study, Kadıoğlu et al. [62] investigated the size-dependent transverse vibration behavior of micromorphic Euler–Bernoulli beams resting on a viscoelastic foundation by employing the nonlocal strain gradient theory. The influence of elastic boundary conditions was also evaluated within the scope of the study. In another study carried out by Mohamed et al. [63], which focused on viscoelastic nanobeams with perforated geometry, a vibration formulation incorporating foundation interaction was developed. Broadening the scope to include complex environmental phenomena, Shakhlavi [64] embedded a ferromagnetic–viscoelastic constitutive relation into the model to gauge the interplay between geometric nonlinearity and axial vibration of nanorods. A similar multiphysics framework was adopted by Abouelregal and Sedighi [65] to study the size-dependent axial dynamics of a rotating viscoelastic nanorod under concurrent magnetic and thermal loads. Furthermore, Gül and Aydoğdu [66] detailed the axial vibration signatures of viscoelastic fiber-reinforced composite nanorods subjected to external damping, again framing their analysis within NET. Deepening the thermodynamic perspective within these size-dependent formulations, Youssef and Alharbi [67] explored the vibrational response of nanobeams under generalized thermoviscoelasticity. Similarly, Abouelregal et al. [68] captured the thermoelectric interactions in viscoelastic microbeams using the size-dependent couple stress model. To account for more complex time-dependent phenomena, Shi and Ma [69] incorporated fractional viscoelasticity and memory effects to assess the magneto-thermoelastic dynamics of rotating nanobeams within a nonlocal framework. Finally, transitioning from one-dimensional elements to two-dimensional biological composites, Moradi et al. [70] evaluated the critical damping and vibrational characteristics of nonlocal lipid/graphene sandwich nanoplates coupled with viscoelastic features.

Presenting a novel perspective, the current study explores the axial vibration characteristics of particle-reinforced nanocomposite structures, integrating the Kelvin–Voigt model to accurately capture the material's intrinsic viscoelastic damping. To account for phenomena occurring at the nanoscale, size effects are embedded into the mathematical framework via the well-established nonlocal elasticity theory (NET). A key departure from the standard rigid-end postulates dominant in existing literature is the implementation of elastic boundary

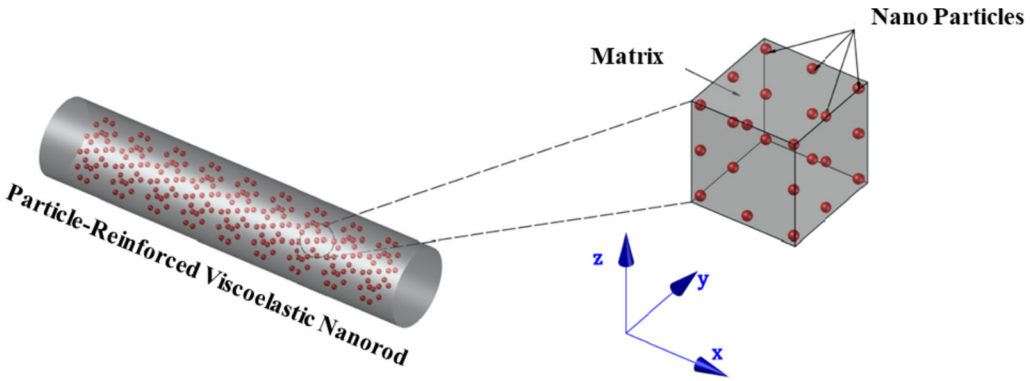


Fig. 2 Homogeneous distributed nanoparticles in matrix

conditions and lumped mass ends, which realistically simulate flexibility at the supports and models attached elemental masses. The study provides closed-form solutions tailored to these compliant boundaries and subsequently extracts the system's vibration frequencies and damping ratios. This comprehensive methodology is expected to establish a theoretical foundation for elucidating the synergistic interaction between particle reinforcement and internal damping, serving as a critical asset in the advanced design of precision nanosensors and NEMS architectures.

2 Particle-reinforced composite material model

In this study, the effective mechanical properties of the particle-reinforced nanocomposite are determined utilizing the Mori–Tanaka model. Although various alternative micromechanical approaches have been recently proposed in the literature [71, 72], the Mori–Tanaka method remains the fundamental cornerstone from which the majority of these modern adaptations are derived. A schematic representation of the two-phase composite structure, consisting of an isotropic matrix and homogeneously distributed spherical isotropic reinforcement particles within this matrix, is presented in Fig. 2.

Within the framework of the Mori–Tanaka micromechanical homogenization technique, the effective bulk modulus (K_C) and the effective shear modulus (G_C) of the composite are expressed as follows [73, 74]:

$$K_C = K_m + \frac{V_r(K_r - K_m)}{1 + (1 - V_r)\frac{K_r - K_m}{K_m + 1.33G_m}} \tag{1}$$

$$G_C = G_m + \frac{V_r(G_r - G_m)}{1 + (1 - V_r)\frac{G_r - G_m}{G_m + f_m}} \tag{2}$$

herein K_m and G_m denote the bulk and shear moduli of the matrix material, respectively, whereas K_r and G_r represent the corresponding moduli for the reinforcement phase. While V_r designates the volume fraction of the reinforcement phase within the composite, the parameter f_m is a coefficient derived from the matrix properties, calculated as follows [73, 74]:

$$f_m = \frac{G_m(9K_m + 8G_m)}{6K_m + 12G_m} \tag{3}$$

Following the determination of the effective bulk and shear moduli of the composite presented in Eqs. (1) and (2), the effective elastic modulus E_c and Poisson's ratio ν_c of the nanocomposite can be obtained utilizing standard isotropic elasticity relations.

$$E_c = \frac{9K_cG_c}{3K_c + G_c} \tag{4}$$

$$\nu_c = \frac{3K_c - 2G_c}{2(3K_c + G_c)} \tag{5}$$

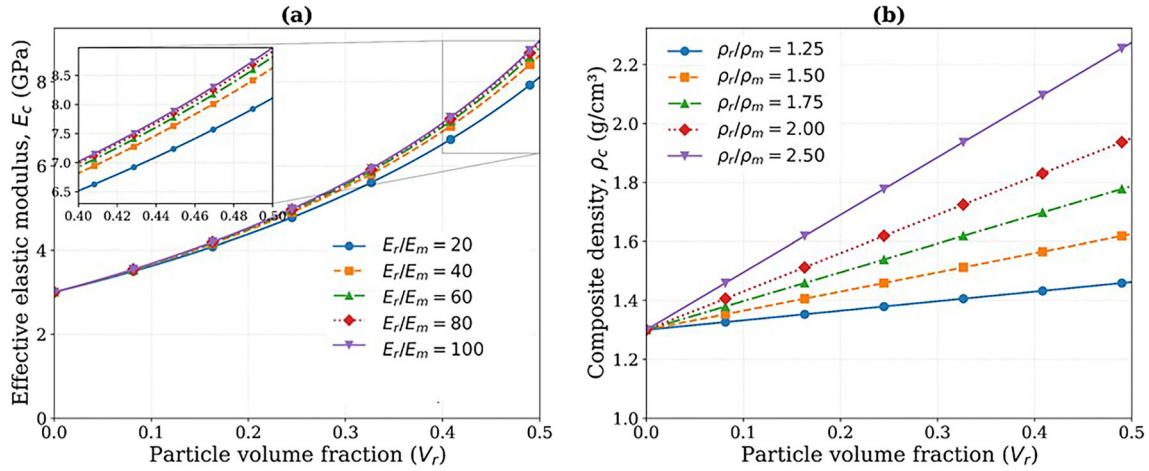


Fig. 3 **a** Effect of elastic modulus ratio and particle volume fraction on effective elastic modulus and **b** effect of density ratio and particle volume fraction on composite density

Within the scope of this study, the mass density of the composite (ρ_c) is calculated utilizing the rule of mixtures, as expressed below [21, 22]:

$$\rho_c = V_r \rho_r + (1 - V_r)\rho_m \tag{6}$$

In Eq. (6), V_r designates the volume fraction of the reinforcement phase within the composite, whereas ρ_r and ρ_m denote the mass densities of the reinforcement and matrix materials, respectively. The variations of the effective elastic modulus and the composite density for the particle-reinforced nanocomposites, over the parameter range considered in the current study, are depicted in Fig. 3. The parameters E_r and E_m presented herein correspond to the elastic moduli of the reinforcement and matrix materials, respectively. The matrix material is assumed to be polyether-ether-ketone (PEEK), and its mechanical properties are therefore treated as constant in the present study. Accordingly, the elastic modulus and mass density of the matrix are specified as $E_m = 3$ GPa and $\rho_m = 1.3$ g/cm^3, respectively [75].

3 Deriving the governing equation

In the present study, a rod manufactured from a particle-reinforced nanocomposite material, possessing a length of L and a uniform cross-sectional area of, is considered. Firstly, the displacements of straight axis axial rod model, homogeneous cross section are given as follows:

$$u_1(x,t) = u(x,t), u_2(x,t) = 0, u_3(x,t) = 0 \tag{7}$$

here $u_1(x,\ t), u_2(x,\ t)$, and $u_3(x,\ t)$ are the displacements of the rod according to x-, y-, and z-axes, respectively. Since Poisson's effect resulting from the axial motion is neglected in the simple axial rod, lateral displacement components $u_2(x,\ t)$ and $u_3(x,\ t)$ are defined as equal to zero. The rod undergoes solely axial vibration along the x-axis, and the axial displacement field is denoted by $u(x,\ t)$ based on the one-dimensional kinematic model, where t represents time. Under the small strain assumption, the axial strain components at any arbitrary point along the rod are defined as follows:

$$\varepsilon_{xx} = \frac{\partial u(x,t)}{\partial x}, \varepsilon_{xy} = \varepsilon_{yx} = \varepsilon_{xz} = \varepsilon_{zx} = \varepsilon_{yz} = \varepsilon_{zy} = \varepsilon_{yy} = \varepsilon_{zz} = 0 \tag{8}$$

Accordingly, the dynamic equilibrium equation for an axially vibrating rod [66] can be modified for composite rod as follows: $\frac{\partial N}{\partial x} = \rho_c A \frac{\partial^2 u(x,t)}{\partial t^2}$. Here, N denotes the normal axial force, expressed with $N = \int_A \sigma_{xx} \mathrm{d}x$.

To account for the internal damping characteristics of the viscoelastic material, the constitutive behavior of the composite structure can be described by the Kelvin–Voigt viscoelastic model. In this model, which relies on the iso-strain principle, the material characteristics are modeled as a parallel spring-dashpot system.

Consequently, the axial stress σ_{xx} within the viscoelastic rod is formulated as a function of both the strain and the strain rate, as given below [76].

$$\sigma_{xx}(x,t) = E_c\varepsilon_{xx} + E_c r_e \frac{\partial \varepsilon_{xx}}{\partial t} \tag{9}$$

In Eq. (9), r_e is referred to as the viscoelastic retardation time and is related to the material-specific viscoelastic coefficient as r_e. Substituting the strain expression derived in Eq. (8) into Eq. (9), the latter can be reformulated as follows:

$$\sigma_{xx}(x,t) = E_c\left(1 + r_e\frac{\partial}{\partial t}\right)\frac{\partial u(x,t)}{\partial x} \tag{10}$$

As previously mentioned, classical continuum mechanics proves inadequate for incorporating factors such as size effects and atomic interactions into the mechanical models of nano- and micro-scale structures. According to the NET proposed by Eringen [30], the stress at any reference point in a body depends not only on the strain at that specific point but also on the strain distribution throughout the entire domain. This phenomenon can be expressed by the following stress–strain equation [30, 31].

$$\sigma^N = \int_V \Xi(|x^{'} - x|, \frac{e_0 a_i}{L}) s_{ij} dV, s_{ij} = \lambda\varepsilon_{rr}\delta_{ij} + 2G\varepsilon_{ij} \tag{11}$$

In the above equation, σ^N, V, Ξ, and $|x^{'} - x|$ are the nonlocal stress tensor, volume, nonlocal module, and distance in the Euclidean form, respectively. s_{ij} is classical stress component with respect to Lamé constants λ and G. Lastly, e_0 is the material-dependent constant and a_i is the internal characteristic length. The integral form of the equation above is cumbersome to use in elasticity problems, and an equivalent differential form of this integral relation, as shown below, is typically used to model different problems:

$$\sigma^N_{xx}(x,t) - \mu\frac{\partial^2\sigma^N_{xx}(x,t)}{\partial x^2} = s_{ij} \tag{12}$$

In Eq. (12), the term μ denotes the nonlocal parameter, which is formulated depending on the material-dependent constant e_0 and the internal characteristic length a_i ($\mu = (e_0 a_i)^2$). If the constitutive relation presented in Eq. (10) for the Kelvin–Voigt viscoelastic model is substituted into the right-hand side of the above equation, the nonlocal viscoelastic constitutive equation is obtained as follows:

$$\sigma^N_{xx}(x,t) - \mu\frac{\partial^2\sigma^N_{xx}(x,t)}{\partial x^2} = E_c\left(1 + r_e\frac{\partial}{\partial t}\right)\frac{\partial u(x,t)}{\partial x} \tag{13}$$

By differentiating Eq. (12) with respect to the spatial coordinate x, the relationship between the variation of stress along the rod and the spatial variations of the displacement field is obtained. Subsequently, using the dynamic equilibrium equation, an equivalent expression is written in place of the spatial derivative of the normal stress. In the final step, both sides of the equation are multiplied by the cross-sectional area A, and thus, the governing differential equation describing the axial vibration behavior of the particle-reinforced viscoelastic nanorod is derived as follows:

$$E_c A\frac{\partial^2 u(x,t)}{\partial x^2} + E_c A r_e\frac{\partial^3 u(x,t)}{\partial x^2\partial t} = \rho_c A\frac{\partial^2 u(x,t)}{\partial t^2} - \mu\rho_c A\frac{\partial^4 u(x,t)}{\partial x^2\partial t^2} \tag{14}$$

Equation (14) indicates that the formulation becomes independent of size effects when the nonlocal parameter is zero, and reduces to a linear elastic structure when the viscoelastic parameter is omitted. Building upon the foundational nonlocal nanorod models in the literature, the present study differentiates itself by introducing a more general and complex boundary condition framework. Specifically, it accounts for the simultaneous attachment of a lumped mass and an elastic spring at the rod's extremity. By combining these advanced boundaries with internal damping via the Kelvin–Voigt model and composite material characteristics through the Mori–Tanaka homogenization scheme, this work provides a versatile and comprehensive dynamic framework for particle-reinforced viscoelastic nanorods. The derived governing partial differential equation is a fourth-order linear homogeneous equation and exhibits a separable structure. By assuming a harmonic motion, the system can be reduced to an ordinary differential equation, the details of which, along with the resulting characteristic equations, are comprehensively presented in the following section.

4 Solving the governing equation

The general solution of the fourth-order governing differential equation for the axial vibration of the viscoelastic nanorod, which incorporates nonlocal effects, can be obtained by employing the separation of variables. Let us assume that the solution $u(x, t)$ is constituted by the product of the separated spatial function $\check{u}(x)$ and the temporal function $g(t)$:

$$u(x,t) = \check{u}(x)g(t) \tag{15}$$

Under the assumption of harmonic vibration, it is evident that the temporal component of the proposed solution will take the form of $g(t) = e^{i\omega t}$. Herein, i equals to $\sqrt{-1}$ and ω denotes the natural vibration frequency. Substituting $u(x, t)$ and its derivatives into Eq. (14) and performing the necessary simplifications yields an ordinary differential equation (ODE) that is dependent solely on the spatial coordinate, as follows:

$$E_c A\frac{\mathrm{d}^2\check{u}(x)}{\mathrm{d}x^2} + i\omega E_c A r_e\frac{\mathrm{d}^2\check{u}(x)}{\mathrm{d}x^2} + \omega^2\rho_c A\check{u}(x) - \mu\omega^2\rho_c A\frac{\mathrm{d}^2\check{u}(x)}{\mathrm{d}x^2} = 0 \tag{16}$$

Rearranging Eq. (16) according to the order of the derivatives yields:

$$\left(E_c A + i\omega E_c A r_e - \mu\omega^2\rho_c A\right)\frac{\mathrm{d}^2\check{u}(x)}{\mathrm{d}x^2} + \omega^2\rho_c A\check{u}(x) = 0 \tag{17}$$

Let us introduce the following non-dimensional parameters to the equation:

$$\xi = \frac{x}{L}; a_n = \frac{\mu}{L^2}; \Omega^2 = \frac{\rho_c A\omega^2 L^2}{E_c A}; \gamma = \omega r_e \tag{18}$$

In this case, the equation transforms into the following form:

$$\left(1 + i\gamma - a_n\Omega^2\right)\frac{\mathrm{d}^2\check{u}(x)}{\mathrm{d}\xi^2} + \Omega^2\check{u}(\xi) = 0 \tag{19}$$

At this stage, to further simplify the equation, let us define a final wave number parameter and express the equation in its simplest form:

$$\begin{gathered}\beta^2 = \frac{\Omega^2}{1 + i\gamma - a_n\Omega^2} \\ \frac{\mathrm{d}^2\check{u}(\xi)}{\mathrm{d}\xi^2} + \beta^2\check{u}(\xi) = 0\end{gathered} \tag{20}$$

The general solution of this second-order linear ordinary differential equation with constant coefficients takes the following form:

$$\check{u}(\xi) = C_1\cos(\beta\xi) + C_2\sin(\beta\xi) \tag{21}$$

The coefficients C_1 and C_2 in Eq. (21) are integration constants determined by applying the kinematic and dynamic boundary conditions at the nanorod ends. While C_1 is typically resolved through displacement constraints (e.g., $C_1 = 0$ for a clamped end), C_2 is incorporated into the dynamic force equilibrium equations to derive the characteristic equations for natural frequencies.

5 Implementing the boundary conditions

In this section, to perform the axial vibration analysis of the particle-reinforced viscoelastic nanorod, five distinct boundary conditions: clamped–clamped (CC), clamped-free (CF), clamped-attached mass (CM), clamped-attached spring (CS) and clamped-attached mass-spring (CMS) representing various physical support configurations are investigated. By adapting the general spatial differential equation solution derived in Eq. (21) to the kinematic and dynamic conditions specific to each boundary condition, the characteristic equations yielding the natural frequencies of the system are derived in an analytical and closed form.

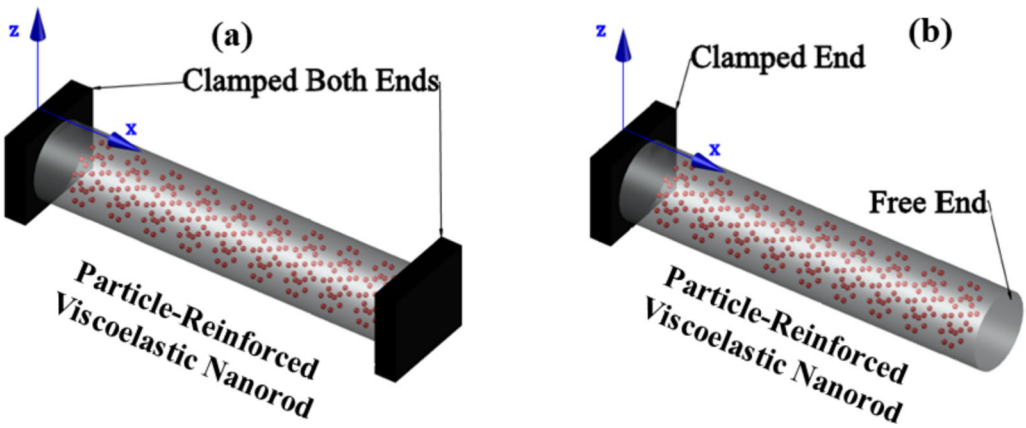


Fig. 4 Particle-reinforced viscoelastic nanorod with CC **a** and CF **b** boundary conditions

5.1 Clamped–clamped ends

For a nanorod clamped at both ends (CC), the boundary conditions require the axial displacement to vanish at both extremities of the rod. The dimensionless boundary conditions for this configuration, the schematic view of which is presented in Fig. 4a, are expressed as follows:

$$\breve{u}(0) = 0; \breve{u}(1) = 0 \tag{22}$$

Applying the boundary condition at the left end ($\breve{u}(0) = 0$) to the general solution (Eq. 21) yields $C_1 = 0$. When the remaining expression $\breve{u}(\xi) = C_2 \sin(\beta\xi)$ is subjected to the boundary condition at the right end ($\breve{u}(1) = 0$) the following equality emerges: $C_2 \sin(\beta\xi) = 0$. For the physical existence of vibration (i.e., a non-trivial solution), the amplitude coefficient must be nonzero $C_2 \neq 0$. Consequently, the equality $\sin(\beta\xi) = 0$ must be satisfied. The roots of this equation yield the analytical solution for the wave number (eigenvalues) for the CC boundary condition as follows:

$$\beta_n = n\pi; (n = 1,2,3\ldots) \tag{23}$$

5.2 Clamped-free ends

For the nanorod model clamped at one end and free at the other (CF), the boundary conditions prescribe zero displacement at the left end and zero normal force (i.e., zero strain) at the right end due to the unconstrained state. The schematic representation of this configuration is provided in Fig. 4b, and its mathematical formulation is expressed as follows:

$$\breve{u}(0) = 0; \frac{\mathrm{d}\breve{u}(1)}{\mathrm{d}\xi} = 0 \tag{24}$$

Deriving from the clamped end condition ($\breve{u}(0) = 0$) $C_1 = 0$ is obtained once again. By taking the first spatial derivative of the solution function and substituting it into the force boundary condition at the right extremity:

$$C_2 \beta \cos(\beta) = 0 \tag{25}$$

Based on the requirement for a non-trivial solution ($C_2 \neq 0$ and $\beta \neq 0$), the roots will be governed by the equation $\cos(\beta) = 0$. Thus, the analytical wave number series (eigenvalues) for the CF boundary condition is obtained as follows:

$$\beta_n = \frac{(2n-1)\pi}{2}; (n = 1,2,3\ldots) \tag{26}$$

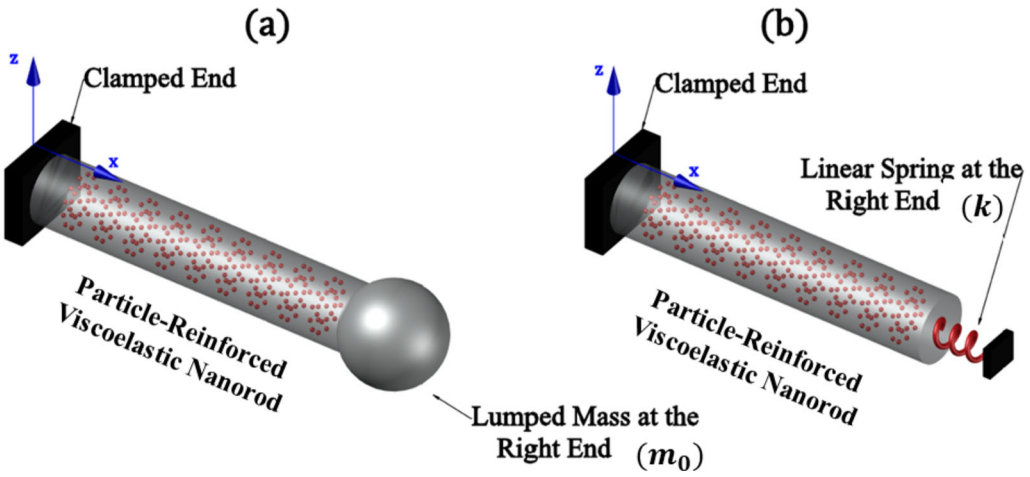


Fig. 5 Particle-reinforced viscoelastic nanorod with CM **a** and CS **b** boundary conditions

5.3 Clamped-lumped mass ends

The schematic representation of the configuration, frequently encountered in practical nanoresonator and mass sensor applications, where the left end is clamped and the right extremity is constrained by a lumped mass, is presented in Fig. 5a. The dynamic boundary conditions for this system are as follows:

$$\breve{u}(0) = 0; \breve{N}(1) = -Z\breve{u}(1) \tag{27}$$

herein letting $M_R = \frac{m_0}{\rho_c AL}$ denote the dimensionless mass parameter representing the lumped mass (m_0), the dimensionless dynamic end impedance encompasses solely the inertial effect and is formulated as $Z = -M_R\Omega^2$. Substituting the dimensionless axial force ($\breve{N}$) expression into the tip boundary condition $\breve{N}(\xi) = \Lambda\frac{\mathrm{d}\breve{u}(\xi)}{\mathrm{d}\xi}$ (where $\Lambda = 1 + i\gamma - a_n\Omega^2$ designates the effective dynamic stiffness parameter).

$$\Lambda\beta C_2\cos(\beta) = -\left(-M_R\Omega^2\right)C_2\sin(\beta) \tag{28}$$

Upon rearranging the equation, the closed-form characteristic equation for the CM boundary condition is derived as follows:

$$\Lambda\beta\cos(\beta) - M_R\Omega^2\sin(\beta) = 0 \tag{29}$$

5.4 Clamped-spring ends

To idealize the interaction of the free end of the nanorod with an elastic medium or an adjacent microcomponent, the clamped-spring boundary condition is established by attaching an elastic spring to the right extremity, as illustrated in Fig. 5b.

The clamped condition at the left end yields $C_1 = 0$'dır. The contribution of the spring component with axial stiffness k at the right end is incorporated into the system through the dimensionless spring stiffness parameter $K_R = \frac{kL}{E_c A}$, which reflects upon the dynamic end impedance as $Z = K_R$. Consequently, the boundary condition assumes the following form: $\breve{N}(1) = K_R\breve{u}(1)$. Substituting the general spatial solution into this dynamic force equilibrium at the right extremity yields the following equality:

$$\Lambda\beta C_2\cos(\beta) = -(K_R)C_2\sin(\beta) \tag{30}$$

Upon simplification of this equation, the characteristic equation for the CS boundary condition is formulated as follows:

$$\Lambda\beta\cos(\beta) + K_R\sin(\beta) = 0 \tag{31}$$

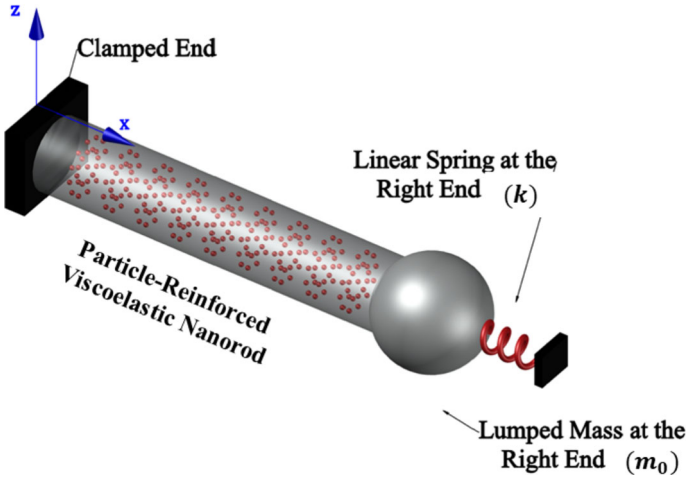


Fig. 6 Particle-reinforced viscoelastic nanorod with CMS boundary conditions

Table 1 Validation for classical boundary conditions (CC, CF)

Boundary condition	Mode number	$a_n = 0$		$a_n = 0.1$		$a_n = 0.2$	
		Ref. [56]	This study	Ref. [56]	This study	Ref. [56]	This study
CC	1	3.14159	3.14159	2.99717	2.99717	2.66009	2.66009
	2	6.28319	6.28318	5.32018	5.32018	3.91239	3.91239
	3	9.42478	9.42478	6.85867	6.85867	4.41692	4.41692
CF	1	1.57080	1.57080	1.55177	1.55177	1.49858	1.49858
	2	4.71239	4.71239	4.26279	4.26279	3.42933	3.42933
	3	7.85398	7.85398	6.17668	6.17668	4.21782	4.21782

5.5 Clamped-lumped mass-spring ends

The most general coupled boundary condition (clamped-mass-spring), wherein both a lumped mass (e.g., a targeted biomolecule) and an elastic constraint (e.g., an interaction with medium or an elastic support) are concurrently present at the right extremity of the nanorod, is illustrated in Fig. 6.

For this complex configuration, the left end is clamped ($C_1 = 0$), and the right end impedance is defined to incorporate both the mass and spring effects as $Z = K_R - M_R\Omega^2$. When the force equilibrium at the right extremity is expressed as $\breve{N}(1) = -\left(K_R - M_R\Omega^2\right)\breve{u}(1)$ and the solution emerging from the right end $\breve{u}(\xi) = C_2\sin(\beta\xi)$ is applied, the equation is formulated as follows:

$$\Lambda\beta C_2\cos(\beta) = -\left(K_R - M_R\Omega^2\right)C_2\sin(\beta) \tag{32}$$

Upon performing the necessary mathematical rearrangements, the universal characteristic equation for the CMS boundary condition is derived as follows:

$$\Lambda\beta\cos(\beta) + \left(K_R - M_R\Omega^2\right)\sin(\beta) = 0 \tag{33}$$

It is noteworthy that this characteristic equation presents a general formulation that encompasses the other configurations introduced in the preceding sections; it reduces to the CS condition for $M_R = 0$, the CM condition for $K_R = 0$, and naturally evolves into the CF characteristic equation when both parameters vanish ($M_R = 0$; $K_R = 0$).

Due to the viscoelastic material properties, all the presented characteristic equations possess complex roots; the real parts of the Ω values obtained from their solution will yield the dimensionless damped natural frequency of the system, whereas the imaginary parts will reflect the viscoelastic damping characteristics. In other words, while the real components determine the oscillation rate of the system, the imaginary components represent the damping capacity, indicating how effectively the material dissipates these vibrations.

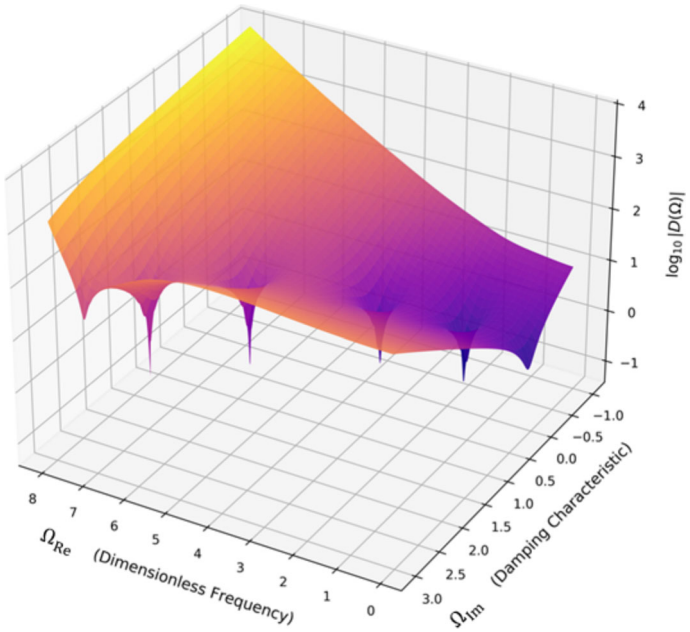


Fig. 7 Characteristic equation determinant surface and complex eigenvalues in complex plane

Table 2 Validation for non-classical boundary conditions (CM, CS, CMS)

Boundary condition	Mode number	$a_n = 0$		$a_n = 0.25$	
		Ref. [56]	This study	Ref. [56]	This study
CM	1	0.86033	0.86033	0.84109	0.84110
$(M_R = 1)$	2	3.42562	3.42562	2.60187	2.60187
	3	6.43730	6.43730	3.39751	3.39751
CS	1	2.02876	2.02876	1.86965	1.86965
	2	4.91318	4.91318	3.16813	3.16813
$(K_R = 1)$	3	7.97867	7.97866	3.61358	3.61359
CMS	1	1.20779	1.20779	1.18033	1.18033
	2	3.44824	3.44824	2.61994	2.61994
$(M_R = K_R = 1)$	3	6.44095	6.44095	3.39956	3.39956

5.6 Deriving the complex roots of the eigenvalue problem

The characteristic equation derived in the preceding sections assumes the form of a nonlinear transcendental equation with complex variables due to the inherent viscoelastic damping effect within the structure. This necessitates seeking the frequency parameter as a complex eigenvalue in the form of $\Omega = \Omega_{\mathrm{Re}} + i\,\Omega_{\mathrm{Im}}$. Herein, Ω_{Re} represents the real part of the eigenvalue, whereas Ω_{Im} denotes the imaginary part of the roots. Since the analytical solution of such complex and transcendental equations is not feasible, high-precision numerical optimization algorithms are employed for the determination of the roots. To mitigate the risk of convergence issues or missing roots associated with direct iterative methods (e.g., pure Newton–Raphson) in such complex problems, a grid search strategy in the complex plane is primarily implemented. Within the defined physical boundaries, the absolute value of the characteristic equation determinant $D|\Omega|$ is evaluated over a high-resolution two-dimensional mesh generated along the Ω_{Re} and Ω_{Im} axes. As observed in the determinant surface plot in the complex plane presented in Fig. 7 the valley or basin points where the surface scanned via grid search approaches zero indicate the estimated root regions satisfying the equation. The surface plot is presented for illustrative purposes to visually verify the distribution of the roots corresponding to different modes of the system in the complex plane and to elucidate the damping–frequency relationship.

Table 3 Comparison of the first three dimensionless complex frequencies for a clamped–clamped viscoelastic nanorod

α_n	Mode number	γ	Ref. [61]		This study	
			Ω_{Re}	Ω_{Im}	Ω_{Re}	Ω_{Im}
0.1	1	0	2.997	0.000	2.997	0.000
		0.01	2.996	0.045	2.997	0.045
		0.02	2.995	0.090	2.996	0.090
		0.03	2.994	0.135	2.994	0.135
		0.04	2.991	0.180	2.992	0.180
		0.05	2.988	0.224	2.989	0.225
0.1	2	0	5.320	0.000	5.320	0.000
		0.01	5.318	0.141	5.318	0.142
		0.02	5.312	0.283	5.313	0.283
		0.03	5.303	0.424	5.303	0.425
		0.04	5.290	0.566	5.290	0.566
		0.05	5.273	0.707	5.273	0.708
0.1	3	0	6.858	0.000	6.859	0.000
		0.01	6.854	0.235	6.855	0.235
		0.02	6.842	0.470	6.843	0.470
		0.03	6.822	0.706	6.822	0.706
		0.04	6.794	0.941	6.794	0.941
		0.05	6.757	1.176	6.757	1.176
0.1732	1	0	2.759	0.000	2.760	0.000
		0.01	2.759	0.038	2.759	0.038
		0.02	2.758	0.076	2.758	0.076
		0.03	2.757	0.114	2.757	0.114
		0.04	2.755	0.152	2.755	0.152
		0.05	2.753	0.190	2.753	0.190
0.1732	2	0	4.251	0.000	4.251	0.000
		0.01	4.250	0.090	4.250	0.090
		0.02	4.247	0.181	4.247	0.181
		0.03	4.242	0.271	4.243	0.271
		0.04	4.236	0.361	4.236	0.361
		0.05	4.227	0.452	4.227	0.452
0.1732	3	0	4.923	0.000	4.923	0.000
		0.01	4.922	0.121	4.922	0.121
		0.02	4.917	0.242	4.917	0.242
		0.03	4.910	0.364	4.910	0.364
		0.04	4.899	0.485	4.899	0.485
		0.05	4.886	0.606	4.886	0.606
0.2236	1	0	2.571	0.000	2.571	0.000
		0.01	2.570	0.033	2.570	0.033
		0.02	2.570	0.066	2.570	0.066
		0.03	2.569	0.099	2.569	0.099
		0.04	2.567	0.132	2.567	0.132
		0.05	2.565	0.165	2.565	0.165
0.2236	2	0	3.643	0.000	3.643	0.000
		0.01	3.643	0.066	3.643	0.066
		0.02	3.641	0.133	3.641	0.133
		0.03	3.638	0.199	3.638	0.199
		0.04	3.634	0.265	3.634	0.266
		0.05	3.628	0.332	3.628	0.332
0.2236	3	0	4.040	0.000	4.040	0.000
		0.01	4.040	0.082	4.040	0.082
		0.02	4.037	0.163	4.037	0.163
		0.03	4.033	0.245	4.033	0.245
		0.04	4.027	0.326	4.027	0.326
		0.05	4.020	0.408	4.020	0.408

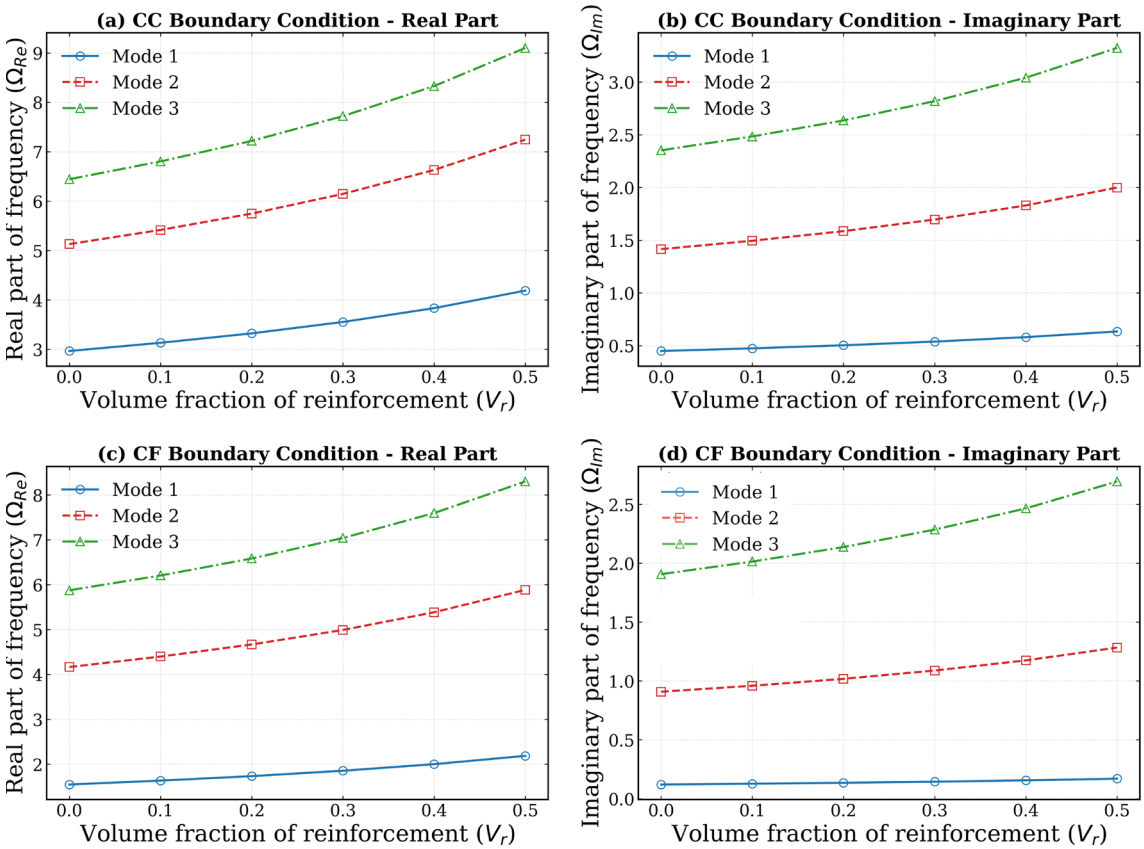


Fig. 8 Effect of particle volume fraction on axial vibration frequency for CC and CF boundary conditions

6 Validation

In Tables 1 and 2, the dimensionless frequency values reported in reference studies for mass-loaded end configurations are compared with the first three modal frequencies obtained utilizing the methodology employed in the current study. In these comparisons, the effect of viscoelasticity and reinforcement are disregarded, and the results corresponding to various values of the nonlocal parameter are tabulated.

To verify the accuracy of the proposed model for the viscoelastic damping case, a comparison study is conducted. The real and imaginary parts of the dimensionless frequencies for the first three modes are presented under the clamped–clamped (CC) boundary condition, considering various values of the dimensionless nonlocal and viscoelastic parameters. The results obtained from the present analytical formulation are compared with those reported by Kadioglu and Yayli [61]. The results presented in this comparison illustrate the vibration of viscoelastic nanorods made of a metallic component. As presented in Table 3, the dimensionless frequencies calculated in this study are in excellent agreement with the reference results, thereby validating the reliability and precision of the current mathematical framework in capturing the dynamic behavior of viscoelastic metallic nanorods.

As can be observed from Tables 1, 2, and 3, the results obtained via the employed root-finding algorithm are in excellent agreement with the nonlocal dimensionless frequencies reported in the literature for the elastic case under various boundary conditions.

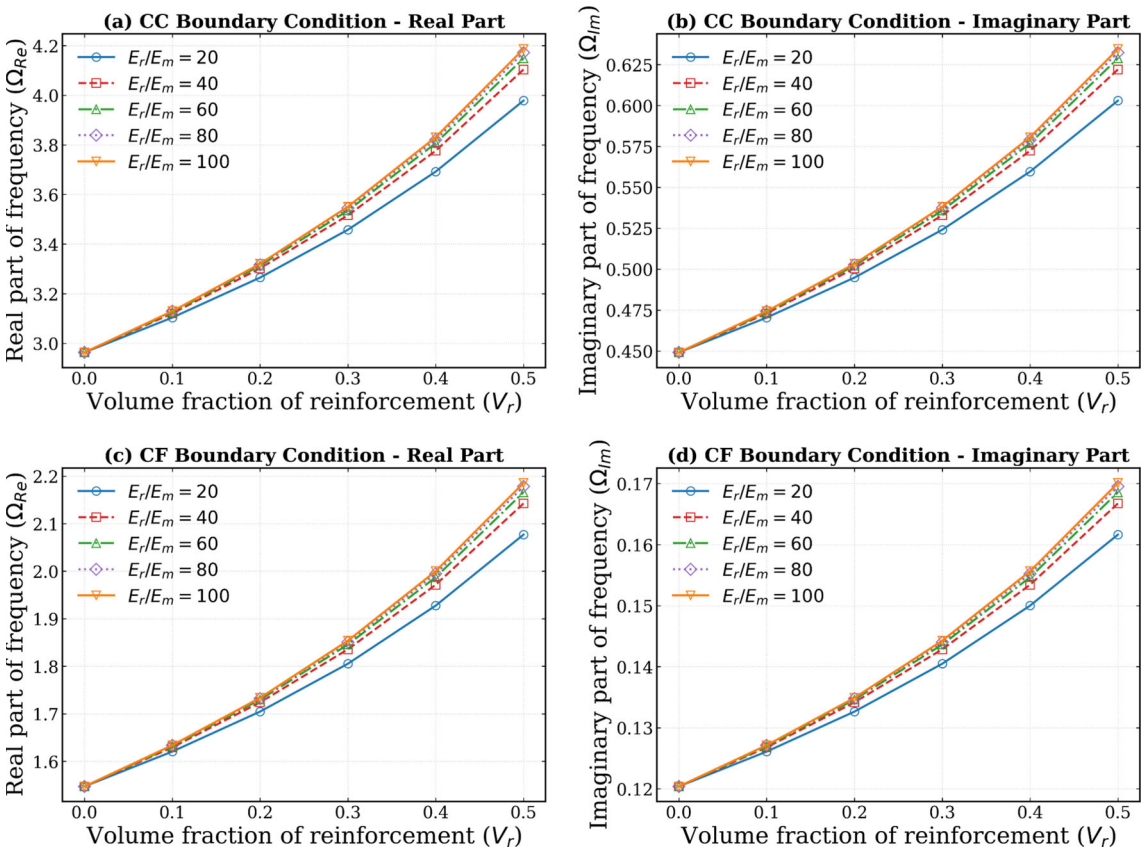


Fig. 9 Effect of $\frac{E_r}{E_m}$ on axial vibration frequency for CC and CF boundary conditions

Table 4 Comparison of the first three dimensionless complex frequencies for a clamped–clamped viscoelastic nanorod

Mode number		1		2		3	
K_R	M_R	Ω_{Re}	Ω_{Im}	Ω_{Re}	Ω_{Im}	Ω_{Re}	Ω_{Im}
0.00	0.00	2.18548	0.17008	5.88343	1.28348	8.29890	2.69471
0.00	1.00	1.20976	0.05190	4.51751	0.74181	7.36095	2.06938
0.00	2.00	0.92039	0.03002	4.36325	0.69073	7.30425	2.03495
0.00	3.00	0.77150	0.02108	4.30678	0.67252	7.28469	2.02316
1.00	0.00	2.82408	0.19170	6.14505	1.28995	8.44413	2.69764
2.00	0.00	3.18151	0.23511	6.36792	1.31599	8.57963	2.71209
3.00	0.00	3.40465	0.28123	6.54728	1.36030	8.69979	2.74235
1.00	1.00	1.69908	0.05273	4.54824	0.74107	7.36548	2.06931
1.00	2.00	1.29901	0.03016	4.37253	0.69060	7.30545	2.03494
1.00	3.00	1.09009	0.02113	4.31116	0.67247	7.28523	2.02316
2.00	1.00	2.06426	0.05562	4.58323	0.73853	7.37026	2.06907
2.00	2.00	1.58722	0.03064	4.38264	0.69016	7.30668	2.03491
2.00	3.00	1.33363	0.02129	4.31580	0.67233	7.28578	2.02314
3.00	1.00	2.36215	0.06110	4.62297	0.73363	7.37529	2.06862
3.00	2.00	1.82801	0.03154	4.39363	0.68933	7.30793	2.03485
3.00	3.00	1.53814	0.02157	4.32076	0.67208	7.28635	2.02313
$K_R \to \infty$	0.00	4.18611	0.63449	7.24473	1.99920	9.10131	3.32263
0.00	$M_R \to \infty$	4.18611	0.63449	7.24473	1.99920	9.10131	3.32263

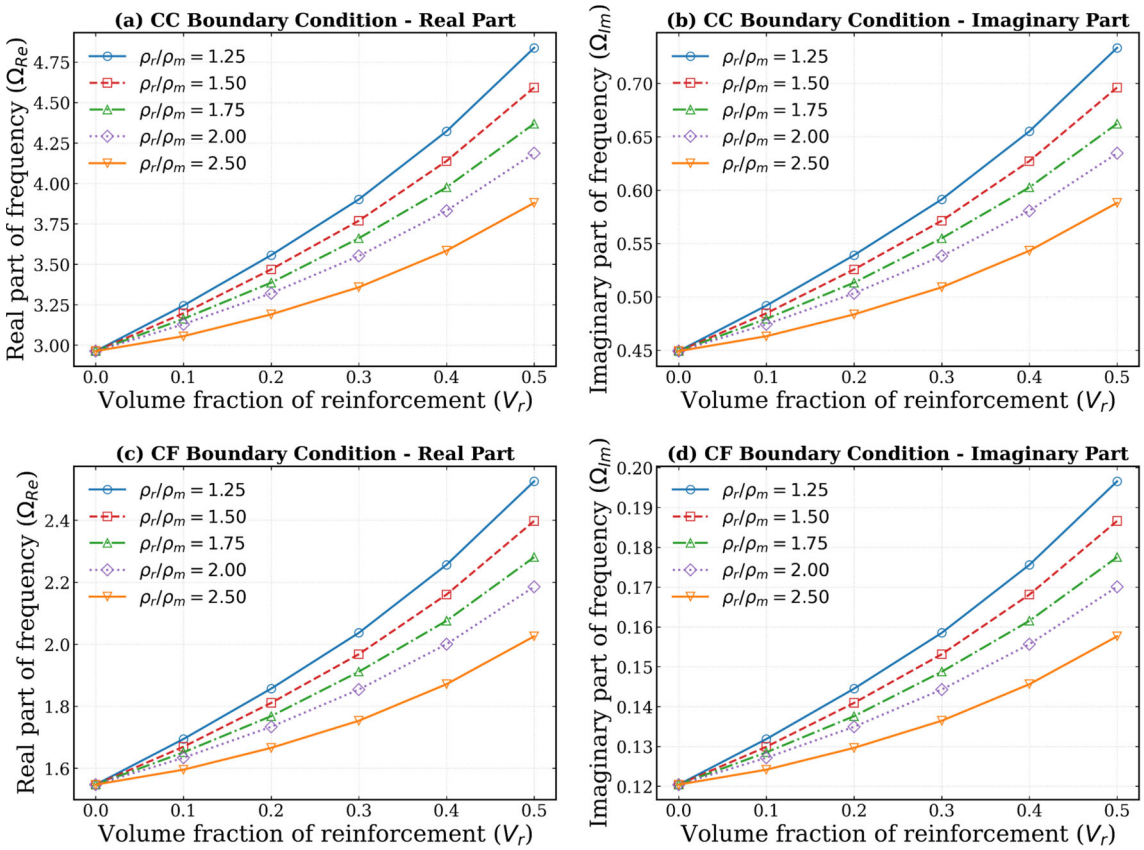


Fig. 10 Effect of $\frac{\rho_r}{\rho_m}$ on axial vibration frequency for CC and CF boundary conditions

7 Results for viscoelastic particle-reinforced nanorod

Within the scope of the present study, the axial vibration frequencies of particle-reinforced nanocomposite rods are investigated, and the obtained results are presented under this section. The elastic and characteristic properties of the matrix material are maintained constant, under the assumption that the matrix is composed of polyether-ether-ketone (PEEK). Accordingly, the elastic modulus and the mass density of the matrix are kept constant at $E_m = 3$ GPa and $\rho_m = 1.3$ g/cm^3 [75], respectively, throughout the study. Furthermore, the length of the nanorod is assumed to be constant at $L = 10$ nm. Unless otherwise specified, the parameters other than the one under observation are kept constant as follows: $\frac{E_r}{E_m} = 100$, $\frac{\rho_r}{\rho_m} = 2.0$, $a_n = 0.1$, $\gamma = 0.1$. It should also be emphasized that the condition $a_n = 0$ reduces the formulation to the classical elasticity theory, whereas the condition $\gamma = 0$ reduces the solutions to the elastic material assumption. However, since performing the computations and generating the graphs in a fully dimensionless form would hinder the observation of the individual effects of the material parameters, a secondary non-dimensionalization procedure compatible with the matrix properties, as defined below, has been implemented, and the results are presented accordingly.

$$\Omega = \omega L \sqrt{\frac{\rho_m}{E_m}} \tag{34}$$

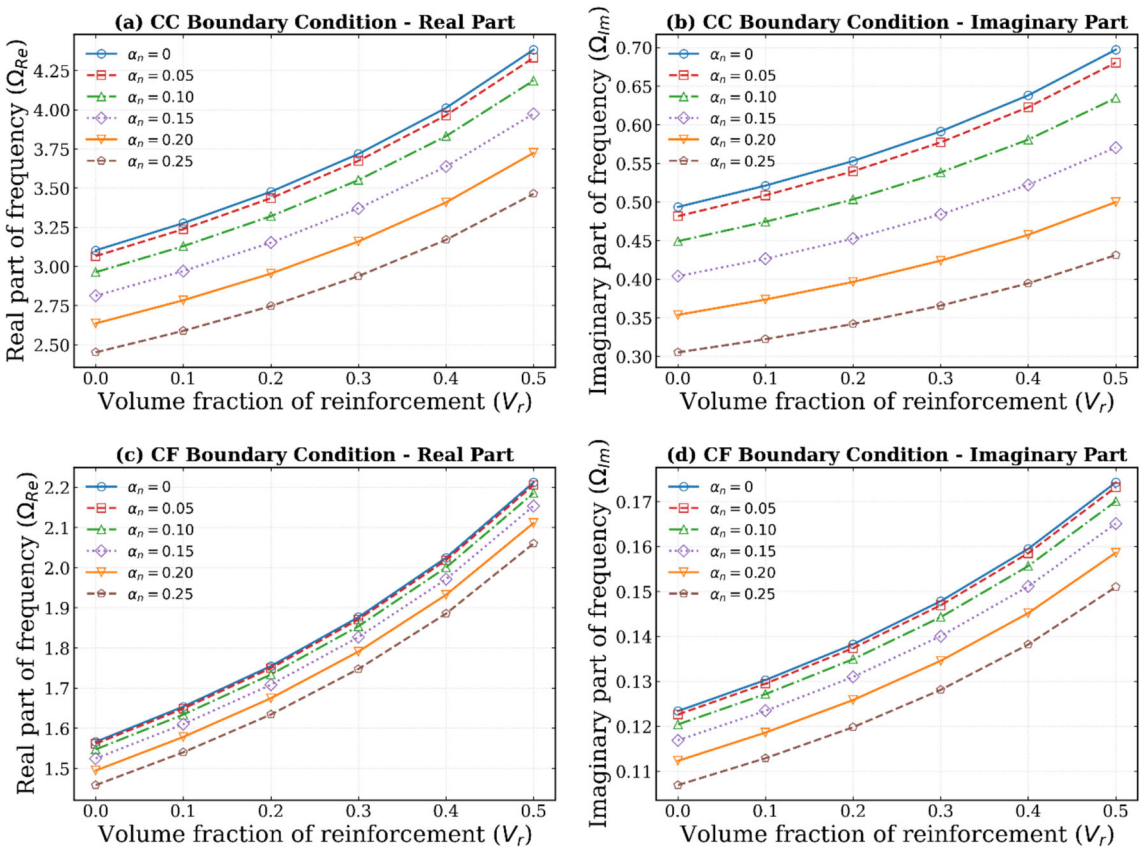


Fig. 11 Effect of a_n on the first axial vibration frequency for CC and CF boundary conditions

7.1 Classical boundary conditions (CC and CF)

Figure 8 presents the natural vibration frequencies of the first three modes obtained at various reinforcement contents V_{r} for the CC and CF boundary conditions. As the composite structure becomes more rigid at higher reinforcement contents, an increase is observed in the natural vibration frequencies of the viscoelastic rod, taking nonlocal effects into account. Compared to the natural vibration frequencies calculated solely for the homogeneous matrix material ($V_{\mathrm{r}} = 0$), the frequencies exhibit an increase of 5.60%, 12.05%, 19.83%, 29.28%, and 41.26% for composites containing particle reinforcement volume fractions of 0.10, 0.20, 0.30, 0.40, and 0.50, respectively. These increments are valid for both the real and imaginary parts of the frequencies. Furthermore, it is observed that this increase is independent of the mode number and boundary conditions.

Figure 9 presents the real and imaginary parts of the natural vibration frequencies obtained at various $\frac{E_r}{E_m}$ ratios and reinforcement contents under the CC and CF boundary conditions. Consistent with the previous analysis, an increase in the natural vibration frequencies is observed in tandem with the increment in reinforcement content. Furthermore, an increase in frequencies occurs as the $\frac{E_r}{E_m}$ ratio increases at different reinforcement contents; however, this enhancement remains quite limited compared to the variation induced by the reinforcement content. For instance, composites with $\frac{E_r}{E_m} = 100$ and a reinforcement volume fraction of 0.50 possess a 5.22% higher natural vibration frequency than composites with $\frac{E_r}{E_m} = 20$ and the same volume fraction. As the reinforcement content decreases, this discrepancy diminishes to even more limited levels. This indicates that within the investigated range, the reinforcement content is a more dominant parameter on the natural vibration frequencies compared to the $\frac{E_r}{E_m}$ ratio. Compared to nanorods composed of the homogeneous matrix material, the frequencies increase by 34.25% in composites containing $\frac{E_r}{E_m} = 20$ and a 0.50 reinforcement volume fraction, whereas this increment is 41.26% for $\frac{E_r}{E_m} = 100$. These ratios are identical across different rigid boundary conditions.

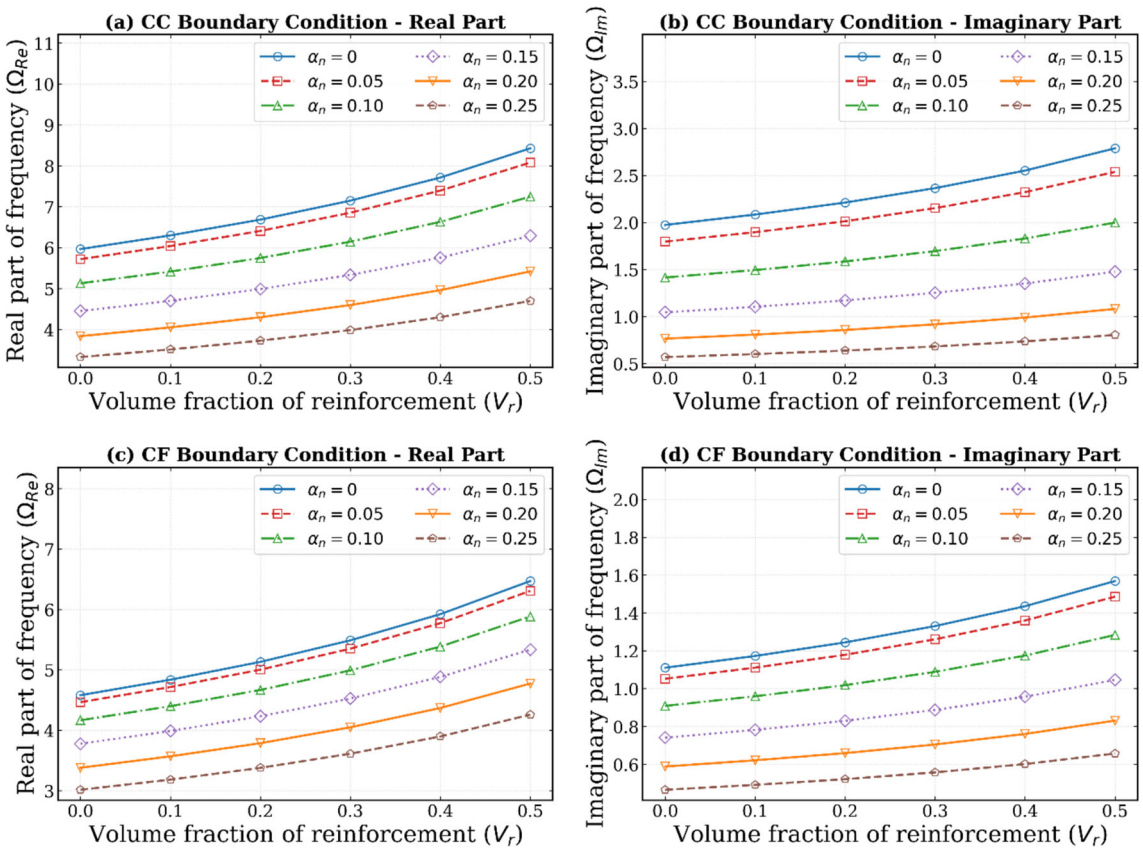


Fig. 12 Effect of a_n on the second axial vibration frequency for CC and CF boundary conditions

Figure 10 illustrates the impact of varying density ratios $\frac{\rho_r}{\rho_m}$ on the fundamental vibration frequencies at different reinforcement contents. An increase in the mass per unit volume of the reinforcement phase elevates the total mass of the system, thereby causing a reduction in the natural vibration frequencies. The elevation of the $\frac{\rho_r}{\rho_m}$ ratio from 1.25 to 2.50 induces a 24.69% decrement in the frequencies at a reinforcement volume fraction of 0.50. The corresponding reduction stands at 16.19% for a volume fraction of 0.30. This observation demonstrates that the influence of the density ratio diminishes as the reinforcement volume fraction decreases.

The value of the nonlocal parameter varies depending on the material's microstructural properties. However, there is no universally accepted fixed value for the nonlocal parameter in the literature for every given material and this parameter is typically determined using experimental data, atomistic models, or molecular dynamics simulations. Therefore, to elucidate the role of small-scale effects on structural behavior, the nonlocal parameter is treated as a variable in this study. The dynamic responses of particle-reinforced viscoelastic nanorods are evaluated comparatively for different nonlocal parameter values. Figure 11 evaluates the combined effects of the reinforcement contents and the variation of the dimensionless nonlocal parameter on the first natural frequency under different boundary conditions. While the influence of the nonlocal parameter on the frequencies remains limited at lower levels, its softening effects become pronounced as the parameter increases. For the first mode under the CC boundary condition, compared to the classical theory, the frequencies decrease by 1.18%, 4.49%, 9.33%, 15.02%, and 20.90% for nonlocal parameter values of $a_n = 0.05, 0.10, 0.15, 0.20$, and 0.25, respectively. Under the CF boundary condition, however, this reduction remains more constrained.

Comparing the second modal frequencies under the CC boundary condition presented in Fig. 12, it is evident that the influence of the nonlocal parameter becomes more pronounced at elevated modes. At identical reinforcement phase contents, the frequencies decrease by 4.13%, 14.02%, 25.38%, 35.68%, and 44.24% compared to the classical theory for parameter values of 0.05, 0.10, 0.15, 0.20, and 0.25, respectively. Moving to the CF boundary condition, this reduction remains at a more limited level, analogous to the observation in the first mode; for nonlocal parameter values of 0.05, 0.10, 0.15, 0.20, and 0.25, the frequencies experience decrements of 1.93%, 6.95%, 13.47%, 20.14%, and 26.25%, respectively.

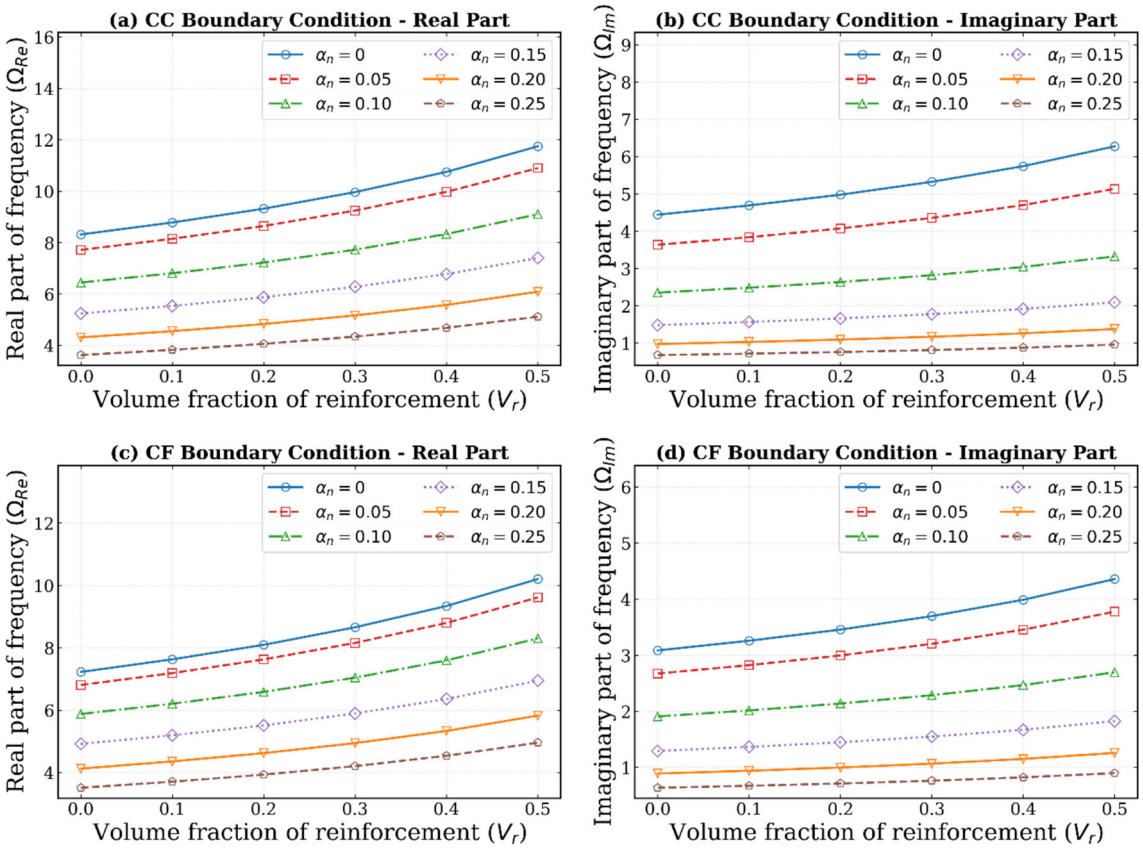


Fig. 13 Effect of a_n on the third axial vibration frequency for CC and CF boundary conditions

Regarding the frequencies pertaining to the third mode presented in Fig. 13, under the CC boundary condition at equivalent reinforcement contents, the frequencies decline by 10.07%, 31.35%, 51.56%, 67.14%, and 78.68% for nonlocal parameter values of 0.05, 0.10, 0.15, 0.20, and 0.25, respectively. Under the CF boundary condition, the natural frequencies belonging to the third mode decrease by 7.01%, 22.60%, 38.68%, 51.97%, and 62.29% compared to the classical theory for the corresponding nonlocal parameter values. Thus, the dominant softening effect of the nonlocal parameter at higher modes is explicitly demonstrated. Furthermore, it is deduced that nonlocal effects play a more critical role under the CC boundary condition.

In Fig. 14, the fundamental angular vibration frequencies of the composite rods are computed at various dimensionless viscous parameters and reinforcement contents. Herein, the existence of the following relationship between the real frequencies obtained from the elastic material Ω_{elastic}, and the real and imaginary parts of the frequencies obtained from the viscoelastic nanorods should be established:

$$\Omega_{\text{elastic}} = \sqrt{\Omega_{\text{Re}}^2 + \Omega_{\text{Im}}^2} \tag{35}$$

here the expressions Ω_{Re} and Ω_{Im} represent the real and imaginary parts of the angular natural vibration frequencies of the viscoelastic nanorod, respectively. An increase in the viscoelastic parameter induces a reduction in the real frequencies while concurrently elevating the imaginary parts. This observation signifies that the wave attenuation capacity of the viscoelastic material is enhanced. Under the CC boundary condition, within the range of $\gamma = 0.05 - 0.25$, the real frequencies decrease between 0.28 and 7.28% compared to the elastic case, whereas under the CF boundary condition, this reduction reaches a maximum level of 1.90%.

Furthermore, Fig. 15 examines the combined effect of the $\frac{E_r}{E_m}$ ratio and the viscoelastic parameter. While maintaining the $\frac{E_r}{E_m}$ ratio constant, an increment in the viscoelastic parameter induces reductions in the natural vibration frequencies on the order of approximately 7% under the CC boundary condition, whereas this difference remains confined to the 1% level under the CF boundary condition.

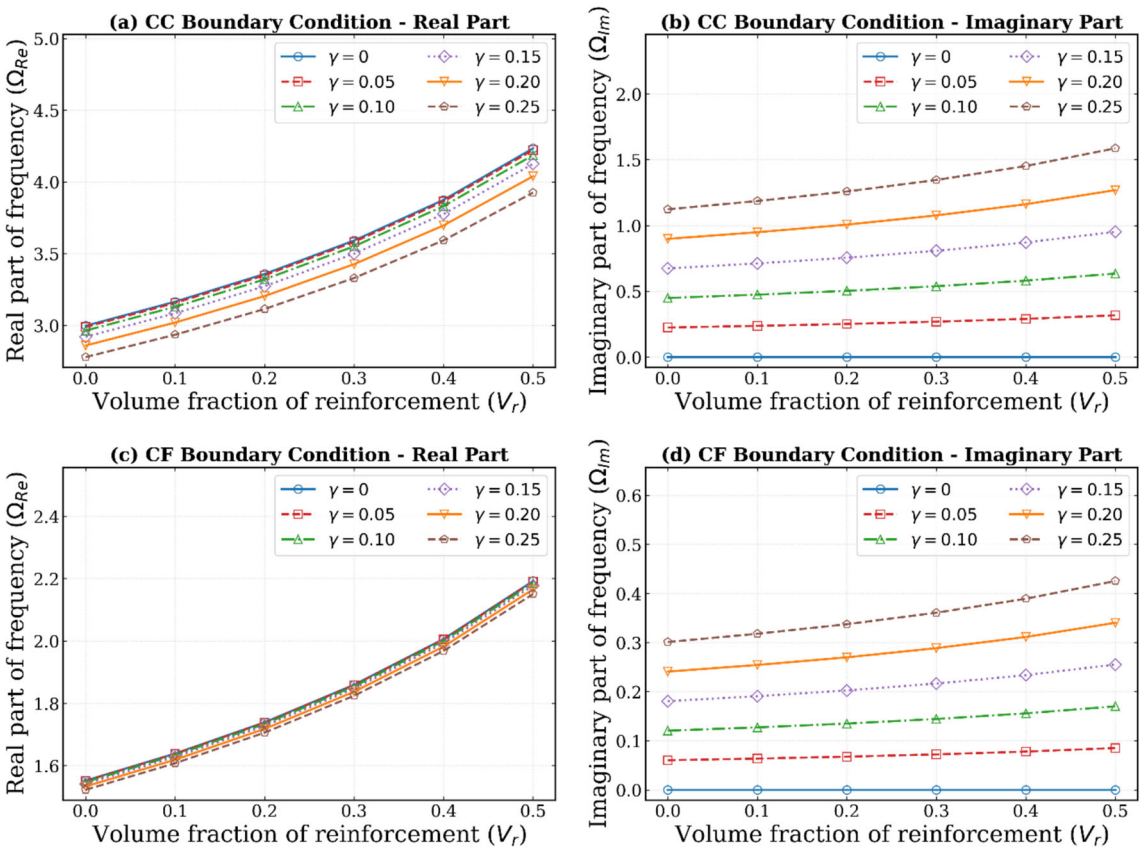


Fig. 14 Effect of γ on axial vibration frequency for CC and CF boundary conditions

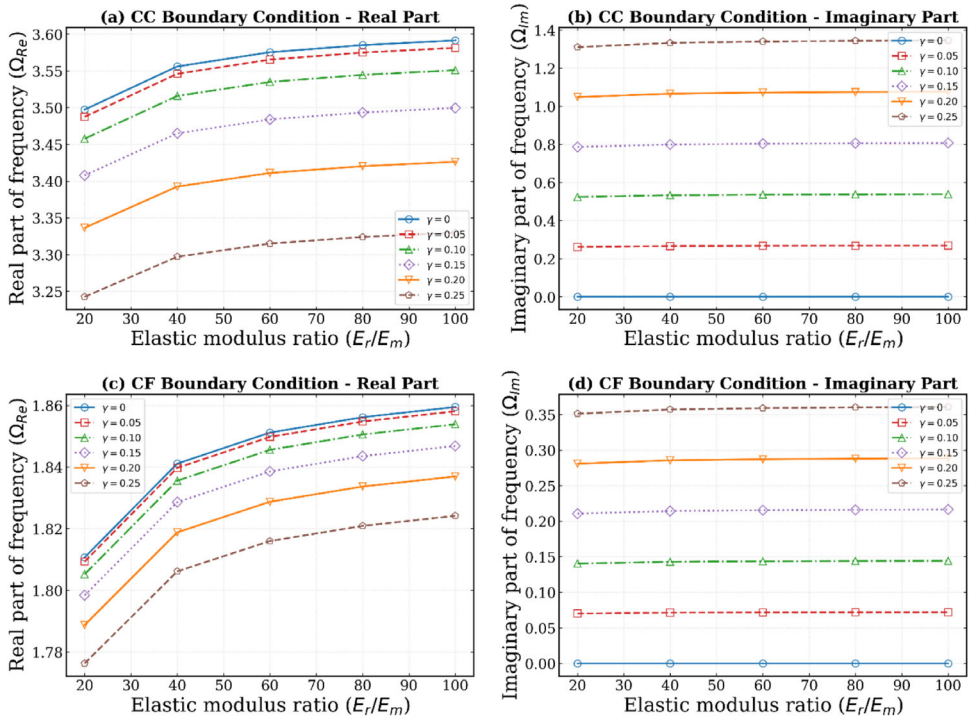


Fig. 15 Effect of $\frac{E_r}{E_m}$ and γ on axial vibration frequency for CC and CF boundary conditions

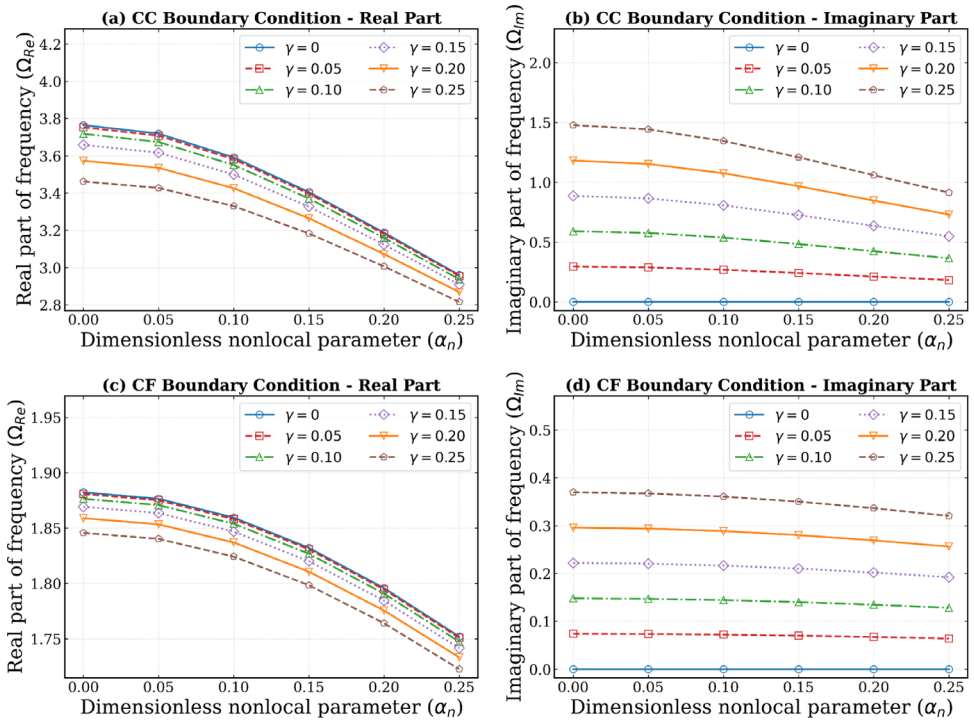


Fig. 16 Effect of a_n and γ on axial vibration frequency for CC and CF boundary condition

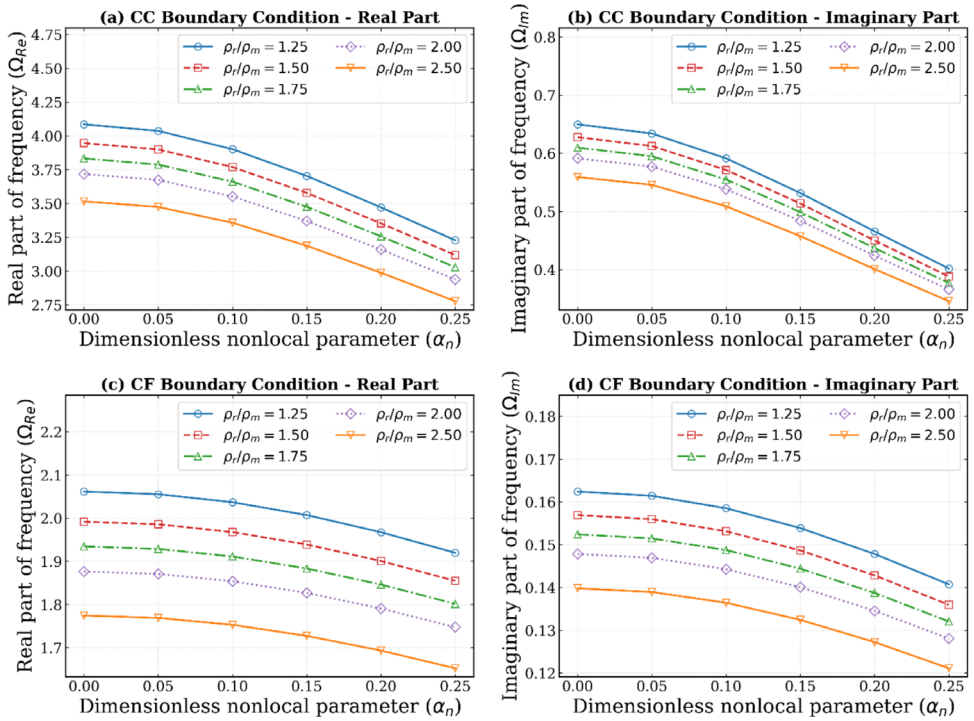


Fig. 17 Effect of a_n and $\frac{\rho_r}{\rho_m}$ on axial vibration frequency for CC and CF boundary conditions

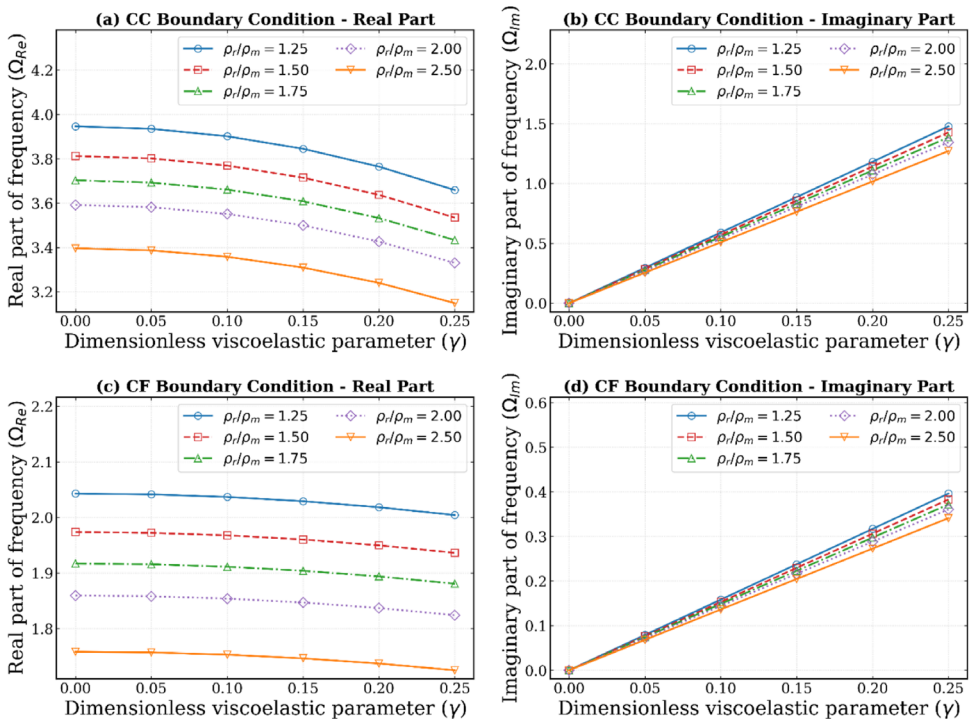


Fig. 18 Effect of γ and $\frac{\rho_r}{\rho_m}$ on axial vibration frequency for CC and CF boundary conditions

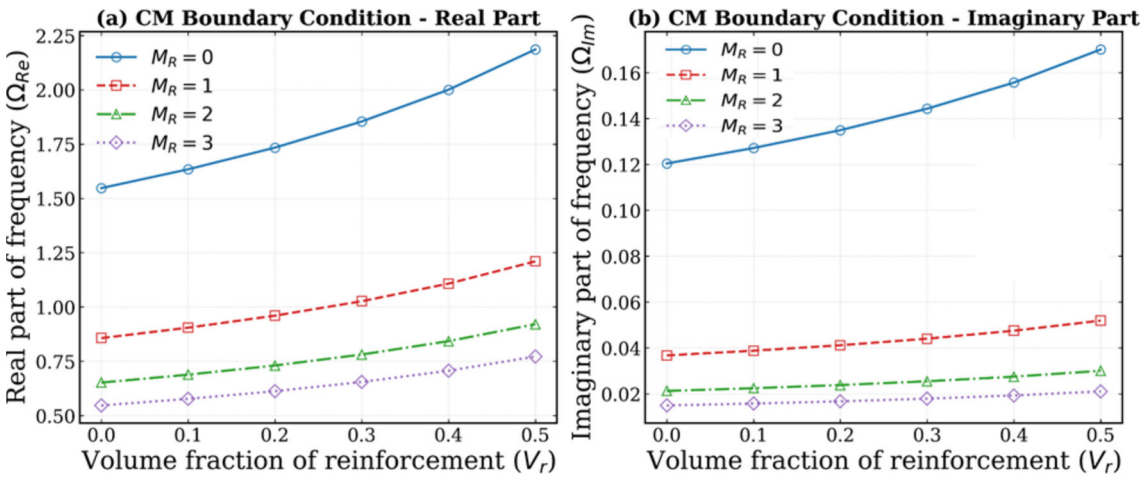


Fig. 19 Effect of M_R on axial vibration frequency of viscoelastic nanorod

Figure 16 investigates the combined effect of the dimensionless nonlocal parameter (a_n) and the viscoelastic parameter (γ). While holding the viscoelastic parameter constant, an increment in the nonlocal parameter leads to a reduction in the frequencies. In instances of high viscoelasticity, the frequency reduction induced by the increment of the nonlocal parameter remains relatively constrained, whereas more pronounced decrements are observed in the elastic state. Under the CC boundary condition, for a constant viscoelastic parameter, an augmentation in the dimensionless nonlocal parameter diminishes the stiffness of the system, thereby causing a decline in the frequencies. At elevated levels of viscoelasticity, the frequency drops associated with an increasing nonlocal parameter are confined to more limited margins; conversely, sharper reductions are evident for nanorods exhibiting low viscoelasticity or perfectly elastic behavior. For instance, when the viscoelastic parameter is 0.25, the fundamental frequencies at a nonlocal parameter of 0.25 are 18.67% lower compared to the classical case where the nonlocal parameter vanishes ($a_n = 0$). In contrast, for the elastic case

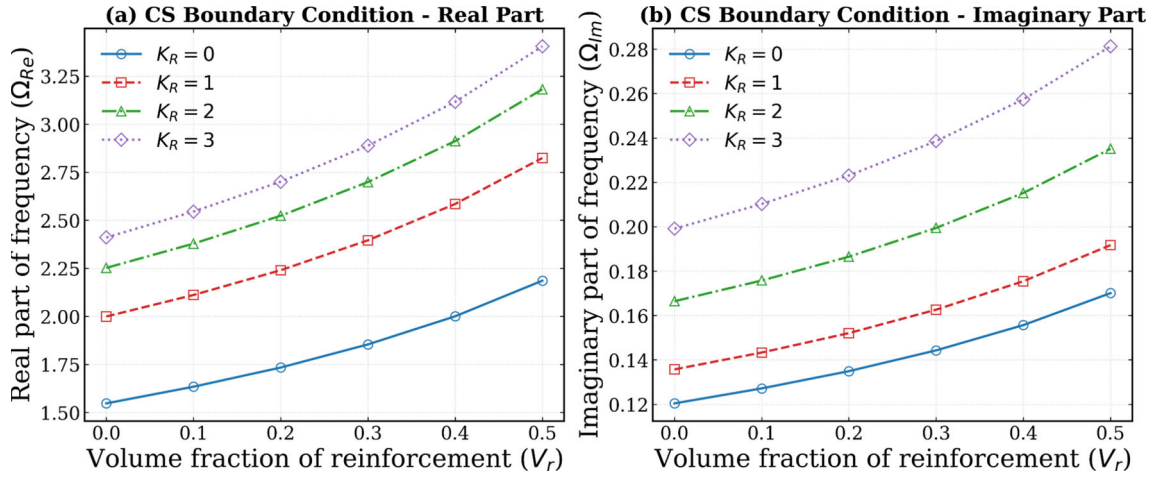


Fig. 20 Effect of K_R on axial vibration frequency of viscoelastic nanorod

(i.e., when the viscoelastic parameter is zero), this reduction is on the order of 21.36%. A similar behavioral trend is observed under the CF boundary condition, although the variations occur within a more restricted range compared to the CC configuration. By way of illustration, for a viscoelastic parameter of 0.25, the fundamental frequencies at a nonlocal parameter of 0.25 decrease by 6.67% relative to the classical case devoid of nonlocal effects, whereas in the elastic state ($\gamma = 0$), this decrement stands at approximately 6.91%.

Figure 17 illustrates the combined effect of the nonlocal parameter and the density ratio $\frac{\rho_r}{\rho_m}$. The softening effect induced by the increment in the nonlocal parameter is distinctly pronounced, and the augmentation in the density ratio elevates the overall mass of the system, thereby resulting in a reduction of the frequencies. These variations are observed to be more prominent under the CC boundary condition. Furthermore, Fig. 18 examines the combined influence of the viscoelastic parameter and the density ratio. An increment in the density ratio brings about a decline in the fundamental frequencies across all levels of the viscoelastic parameter.

7.2 Clamped, spring, and lumped mass-attached boundary conditions (CS, CM, CMS)

In this section, for the case where the dimensionless nonlocal parameter ($a_n = 0.10$) and the viscoelastic damping coefficient ($\gamma = 0.10$) are assumed to be constant, the effects of the reinforcement phase volume fraction within the composite structure (V_r), the dimensionless lumped mass attached to the right end (M_R), and the dimensionless spring stiffness (K_R) on the complex natural vibration frequencies of the system are investigated. To observe the interactions at the physical boundary conditions more clearly, the results are presented in Figs. 19, 20, and 21 for cases with solely an attached mass (CM), solely an attached spring (CS), and a mass-spring combination (CMS), taking into account the variation of the reinforcement ratio (V_r) on the horizontal axis. In all scenarios, the increment of V_r generally elevates both the real (Ω_{Re}) and imaginary (Ω_{Im}) frequency components. This is attributed to the fact that the highly rigid nano-reinforcement elements embedded into the matrix enhance the total effective stiffness of the system. The characteristic effects of the boundary conditions are detailed below:

7.2.1 Analyses for the case with only a tip mass (CM)

The analyses pertaining to the configuration where no spring is present at the right end ($K_R = 0$) and the lumped mass (M_R) is varied are depicted in Fig. 19. In the limiting case ($M_R \to 0$), the system converges to the classical clamped-free (CF) boundary conditions. An increase in the amount of lumped mass attached to the tip amplifies the inertial effect at that point, thereby reducing the vibration frequencies of the rod. For instance, in the case of a pure polymer matrix where no reinforcement phase has yet been introduced ($V_r = 0$), the real frequency value of the rod without a tip mass ($M_R = 0$) is 1.547; however, when the mass parameter is raised to the $M_R = 3$ level, this value drops to 0.546, exhibiting a pronounced decrement of approximately 64.7%. When the imaginary frequency components are examined, it is determined that the inertial increase

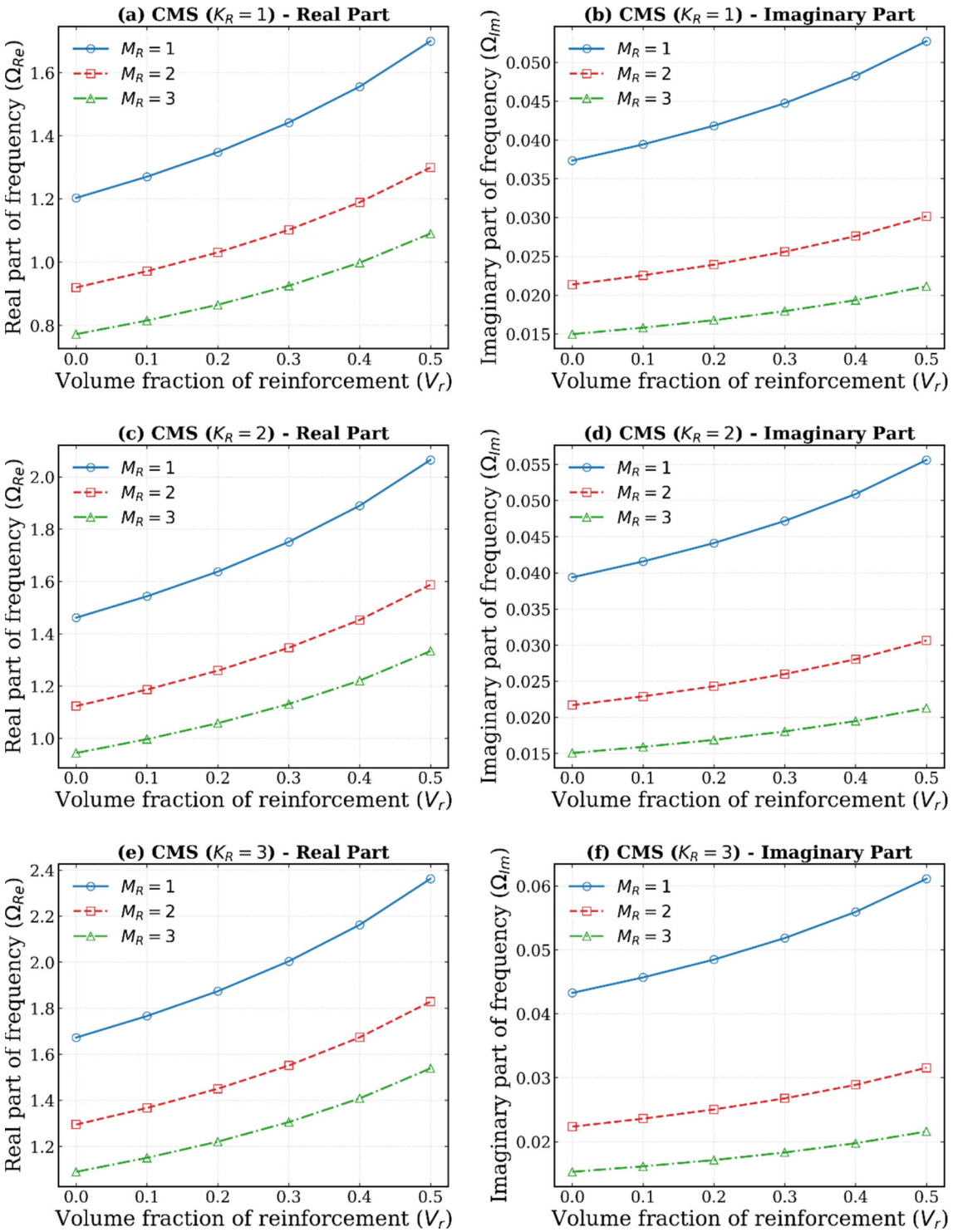


Fig. 21 Unified effect of M_R and K_R on axial vibration frequency of viscoelastic nanorod

at the tip attenuates the damping capability of the system. It is observed that this ratio is independent of the reinforcement content.

7.2.2 Analyses for the case with only an axial spring (CS)

The results for the case where solely the axial linear spring is effective ($M_R = 0$) are presented in Fig. 20. Theoretically, as the spring stiffness approaches infinity($K_R \to \infty$), the system reverts to the clamped–clamped (CC) condition. Contrary to the mass, the linear spring attached to the system generates a structural resistance at the boundary point, thereby increasing the total effective stiffness and elevating the natural frequencies. Taking the $K_R = 0$ initial state as a baseline, the real frequency value, which is 1.547 for $V_r = 0$, reaches 2.410 at the $K_R = 3$ level, exhibiting an increment of approximately 55.8%. Additionally, this increase in spring stiffness leads to an augmentation in the imaginary component, indicating that the boundary stiffness and the viscoelastic characteristic mutually support one another.

7.2.3 Analyses for the complex mass-spring case (CMS)

The results pertaining to the complex configurations where both the spring and the mass are simultaneously present at the right end (CMS) are presented in Fig. 21. In this configuration, the stiffening tendency of the spring and the frequency-lowering inertial effects of the mass compete with each other. However, the results reveal that even at high spring stiffness levels, the frequency-reducing effect of the mass increment (inertial force) is highly dominant. For instance, at a relatively rigid boundary support such as $K_R = 3$ and in the pure matrix state ($V_r = 0$), the real frequency of 2.410 obtained when there is no tip mass ($M_R = 0$) drops to 1.08884 when a mass of $M_R = 3$ is attached to the same spring, experiencing a reduction of approximately 54.8%. Nevertheless, this drastic drop can be partially compensated by the reinforcement phase added to the composite structure and the enhancement of the boundary spring. Even in the case of the heaviest tip mass attachment ($M_R = 3$), elevating the spring stiffness from $K_R = 1$ to $K_R = 3$ raises the real frequencies from 0.77169 to 1.08884, providing an improvement of 41.10%. Similarly, increasing the reinforcement content imparts additional inherent stiffness to the system. For example, in the case of $M_R = K_R = 3$, the real frequency value, which is 1.08884 for the nanorod composed entirely of the homogeneous matrix ($V_r = 0$), is observed as 1.538140 for the rod with a 50% reinforcement content ($V_r = 0.50$), indicating an increment of 41.26%.

To provide a quantitative summary of the combined influence of the attached mass and spring parameters on the damped natural frequencies at a fixed reinforcement level, the first dimensionless complex frequency values obtained for the particle-reinforced viscoelastic nanorod with a particle volume fraction of $V_r = 0.50$ are listed in Table 4. Remaining parameters are held constant at $\frac{E_r}{E_m} = 100$, $\frac{\rho_r}{\rho_m} = 2.0$, $a_n = 0.1$, $\gamma = 0.1$. The case $K_R = M_R = 0$ corresponds to the classical clamped-free (CF) configuration, while the remaining rows refer to clamped-mass (CM), clamped-spring (CS), and clamped-mass-spring (CMS) boundary conditions as analyzed in Sect. 7.2. In the limiting cases, $K_R \to \infty$ and $M_R \to \infty$ recover the clamped–clamped (CC) boundary condition.

8 Conclusion

In this study, the axial vibration behaviors of particle-reinforced viscoelastic nanorods are comprehensively investigated within the framework of Eringen's nonlocal elasticity theory and the Kelvin–Voigt viscoelastic damping model. The effective material properties of the composite nanorod are modeled utilizing the Mori—Tanaka homogenization scheme. The complex natural vibration frequencies of the system are analytically formulated and obtained via a high-precision numerical root-finding algorithm under classical, mass-attached (CM), spring-attached (CS), and complex mass-spring-attached (CMS) boundary conditions. The principal findings derived from the conducted parametric analyses are summarized below:

- *Effect of reinforcement content* An increase in the volume fraction of the particle reinforcement embedded within the matrix significantly enhances the effective stiffness of the system (stiffening effect), thereby leading to an elevation in the natural vibration frequencies.
- *Effect of the nonlocal parameter* The increment of the nonlocal parameter induces a softening effect on the nanorod structure, resulting in a reduction in the frequencies. This effect is determined to be substantially more dominant at higher vibration modes and under the clamped–clamped (CC) boundary condition.

- *Effect of viscoelasticity* An augmentation in the viscoelastic damping parameter causes a decrease in the real parts of the natural frequencies while concurrently elevating the imaginary parts (damping characteristics). This phenomenon is directly associated with the enhanced wave attenuation capacity of the viscoelastic material.
- *Effect of the density ratio* An increase in the density ratio of the reinforcement phase relative to the matrix elevates the total inertia of the system, consequently leading to a decline in the natural frequencies.
- *Boundary conditions and interactions* While an attached tip mass amplifies the inertial effects and lowers the frequencies, an elastic spring generates structural resistance and raises the frequencies. In complex configurations where both mass and spring are simultaneously present (CMS), it is revealed that the frequency-reducing effect of the mass increment remains highly dominant even at elevated spring stiffness levels.

These obtained analytical and numerical findings provide a robust theoretical foundation for the dynamic analysis and design optimization of next-generation nano-electro-mechanical systems (NEMS), dampers, nanoresonators, and high-precision mass sensors.

Author contributions A.B.C. helped in conceptualization, investigation, data curation, formal analysis, methodology, validation, visualization, writing—original draft. B.U. contributed to conceptualization, investigation, formal analysis, methodology, validation, supervision, visualization, writing—original draft.

Funding Open access funding provided by the Scientific and Technological Research Council of Türkiye (TÜBİTAK).

Data availability No datasets were generated or analyzed during the current study.

Declarations

Conflict of interest The authors declare no competing interests.

Open Access This article is licensed under a Creative Commons Attribution 4.0 International License, which permits use, sharing, adaptation, distribution and reproduction in any medium or format, as long as you give appropriate credit to the original author(s) and the source, provide a link to the Creative Commons licence, and indicate if changes were made. The images or other third party material in this article are included in the article's Creative Commons licence, unless indicated otherwise in a credit line to the material. If material is not included in the article's Creative Commons licence and your intended use is not permitted by statutory regulation or exceeds the permitted use, you will need to obtain permission directly from the copyright holder. To view a copy of this licence, visit http://creativecommons.org/licenses/by/4.0/.

References

1. Iijima, S.: Helical microtubules of graphitic carbon. Nature **354**, 56–58 (1991). https://doi.org/10.1038/354056A0
2. Kumar, E.K., Meher, A.K., Kumar, V., Panda, S.K.: Application of functionally graded nano- and microstructures in biomedical devices. Adv. Model. Anal. Functionally Graded Micro- Nanostruct. **9**(1), 9–12 (2024). https://doi.org/10.1088/978-0-7503-6024-1CH9
3. Krishna, S.B.N., Jakmunee, J., Mishra, Y.K., Prakash, J.: ZnO based 0–3D diverse nano-architectures, films and coatings for biomedical applications. J. Mater. Chem. B **12**, 2950–2984 (2024). https://doi.org/10.1039/D4TB00184B
4. Ozalp, A.F., Esen, I.: Magnetic field effects on the thermomechanical vibration behavior of functionally graded biocompatible material sandwich nanobeams. Mech. Adv. Mater. Struct. **32**, 459–477 (2025). https://doi.org/10.1080/15376494.2024.2349966
5. Wang, W., Yang, R., Liu, M.: Design and fabrication of micro/nano sensors and actuators. Micromachines (2024). https://doi.org/10.3390/MI15060674
6. Karaca, M.M., Esen, I.: On the effect of foam structures on thermo-mechanical vibration response of functionally graded piezoelectric smart plates. Int. J. Mech. Mater. Des. **21**(4), 849–875 (2025). https://doi.org/10.1007/S10999-025-09755-7
7. Paliwal, G., Bunglowala, A.: Nanosensor and actuator technologies for wearable mobile patient monitoring systems: a review. Springer Proc. Math. Stat. **342**, 83–95 (2021). https://doi.org/10.1007/978-981-15-9708-4_7
8. Qu, G., Xia, H., Liang, Q., Liu, Y., Ming, S., Zhao, J., Xia, Y., Wu, J.: Current research status and future trends of vibration energy harvesters. Micromachines (2024). https://doi.org/10.3390/mi15091109
9. Feng, H., Bu, L., Ling, Y., Jiang, S., Zhao, X., Li, Z., Xu, M., Xu, S., Wang, X.: A heterogeneous cascaded resonant MEMS energy harvester with in situ integrated PVDF films for sub-10 Hz ultra-low-frequency vibration energy harvesting. Small **21**, 2504771 (2025). https://doi.org/10.1002/smll.202504771
10. Ning, S., Zhu, H., Feng, C., Gu, J., Jiang, Z., Ying, Z., Midkiff, J., Jain, S., Hlaing, M.H., Pan, D.Z., Chen, R.T.: Photonic-electronic integrated circuits for high-performance computing and AI accelerators. J. Lightwave Technol. **42**, 7834–7859 (2024). https://doi.org/10.1109/JLT.2024.3427716

11. Lu, S., Cheng, Y., Wang, Y., Wang, R.: Folivora: ultra low power microprocessor design with nano electro-mechanical relay and nanotube memory. IEEE Trans. Comput. Aided Des. Integr. Circuits Syst. (2025). https://doi.org/10.1109/TCAD.2025.3630558
12. Mindlin, R.D., Eshel, N.N.: On first strain-gradient theories in linear elasticity. Int. J. Solids Struct. **4**, 109–124 (1968). https://doi.org/10.1016/0020-7683(68)90036-X
13. Lam, D.C.C., Yang, F., Chong, A.C.M., Wang, J., Tong, P.: Experiments and theory in strain gradient elasticity. J. Mech. Phys. Solids **51**, 1477–1508 (2003). https://doi.org/10.1016/S0022-5096(03)00053-X
14. Yang, F., Chong, A.C.M., Lam, D.C.C., Tong, P.: Couple stress based strain gradient theory for elasticity. Int. J. Solids Struct. **39**, 2731–2743 (2002). https://doi.org/10.1016/S0020-7683(02)00152-X
15. Gurtin, M.E., Ian Murdoch, A.: A continuum theory of elastic material surfaces. Arch. Ration. Mech. Anal. **57**, 291–323 (1975). https://doi.org/10.1007/BF00261375
16. Hamilton, J.C., Wolfer, W.G.: Theories of surface elasticity for nanoscale objects. Surf. Sci. **603**, 1284–1291 (2009). https://doi.org/10.1016/j.susc.2009.03.017
17. Dorduncu, M., Ren, H., Zhuang, X., Silling, S., Madenci, E., Rabczuk, T.: A review of peridynamic theory and nonlocal operators along with their computer implementations. Comput. Struct. **299**, 107395 (2024). https://doi.org/10.1016/j.compstruc.2024.107395
18. Madenci, E., Oterkus, E.: Peridynamic theory. Peridyn Theory Appl. (2014). https://doi.org/10.1007/978-1-4614-8465-3_2
19. Akbaş, ŞD., Dastjerdi, S., Akgöz, B., Civalek, Ö.: Dynamic analysis of functionally graded porous microbeams under moving load. Transp. Porous Media **142**, 209–227 (2022). https://doi.org/10.1007/s11242-021-01686-z
20. Uzun, B., Yayli, M.Ö.: A unified technique for stability analysis of an embedded FG porous nano/microbeam via modified couple stress theory. Nano **19**, 2450072 (2024)
21. Abdelrahman, A.A., Esen, I., Daikh, A.A., Eltaher, M.A.: Dynamic analysis of FG nanobeam reinforced by carbon nanotubes and resting on elastic foundation under moving load. Mech. Based Des. Struct. Mach. **51**, 5383–5406 (2023). https://doi.org/10.1080/15397734.2021.1999263
22. Civalek, Ö., Akgöz, B.: Bending analysis of CNT-reinforced composite strain gradient microbeams. Mech. Res. Commun. **148**, 104502 (2025). https://doi.org/10.1016/j.mechrescom.2025.104502
23. Alibakhshi, A., Dastjerdi, S., Akgöz, B., Civalek, Ö.: Parametric vibration of a dielectric elastomer microbeam resonator based on a hyperelastic cosserat continuum model. Compos. Struct. **287**, 115386 (2022). https://doi.org/10.1016/j.compstruct.2022.115386
24. Uzun, B., Civalek, Ö., Yaylı, M.Ö.: A hardening nonlocal approach for vibration of axially loaded nanobeam with deformable boundaries. Acta Mech. **234**, 2205–2222 (2023). https://doi.org/10.1007/s00707-023-03490-w
25. Eroğlu, M., Esen, İ, Koç, M.A.: The effect of the viscoelastic support and GRPL-reinforced foam material on the thermomechanical vibration response of piezomagnetic sandwich nanosensor plates. Acta Mech. **235**, 2415–2453 (2024). https://doi.org/10.1007/s00707-023-03843-5
26. Yıldız, T., Esen, I.: On the effect of the Casimir, van der Waals and electrostatic forces on the thermomechanical buckling of sandwich smart piezo magnetic nanosensor/switch plates. Microsyst. Technol. **31**, 1525–1545 (2025). https://doi.org/10.1007/s00542-024-05813-w
27. Aktaş, K.G., Esen, İ: Dynamic response analysis and active vibration control of the smart sandwich composite plate with FGM core layers and MIMO FGPM actuators and sensors. Int. J. Mech. Syst. Dyn. **5**, 3–19 (2025). https://doi.org/10.1002/msd2.70001
28. Kafali, A., Buğday, M., Esen, I.: Wave propagation behavior of sandwich nanoplates with butterfly auxetic metamaterial core layer and graphene-reinforced foam FGM face layers. ZAMM Z. Angew. Math. Mech. **106**, e70360 (2026). https://doi.org/10.1002/zamm.70360
29. Moradi, A., Ghanbarzadeh, A., Shishesaz, M., Sedighi, H.M.: Nonlinear vibration and primary resonance analysis of porous FG/Lipid sandwich bionanoplates based on nonlocal strain gradient theory. Acta Mech. **236**, 1029–1059 (2025). https://doi.org/10.1007/s00707-024-04132-5
30. Eringen, A.C., Edelen, D.G.B.: On nonlocal elasticity. Int. J. Eng. Sci. **10**, 233–248 (1972). https://doi.org/10.1016/0020-7225(72)90039-0
31. Eringen, A.C.: On differential equations of nonlocal elasticity and solutions of screw dislocation and surface waves. J. Appl. Phys. **54**, 4703–4710 (1983). https://doi.org/10.1063/1.332803
32. Ebrahimi, F., Barati, M.R.: Hygrothermal buckling analysis of magnetically actuated embedded higher order functionally graded nanoscale beams considering the neutral surface position. J. Therm. Stress. **39**, 1210–1229 (2016). https://doi.org/10.1080/01495739.2016.1215726
33. Nazemnezhad, R., Hosseini-Hashemi, S.: Nonlocal nonlinear free vibration of functionally graded nanobeams. Compos. Struct. **110**, 192–199 (2014)
34. Li, Y.S., Cai, Z.Y., Shi, S.Y.: Buckling and free vibration of magnetoelectroelastic nanoplate based on nonlocal theory. Compos. Struct. **111**, 522–529 (2014)
35. Ebrahimi, F., Barati, M.R.: Buckling analysis of piezoelectrically actuated smart nanoscale plates subjected to magnetic field. J. Intell. Mater. Syst. Struct. **28**, 1472–1490 (2017). https://doi.org/10.1177/1045389X16672569
36. Van Vinh, P., Tounsi, A., Belarbi, M.O.: On the nonlocal free vibration analysis of functionally graded porous doubly curved shallow nanoshells with variable nonlocal parameters. Eng. Comput. **39**, 835–855 (2023). https://doi.org/10.1007/s00366-022-01687-6
37. Tran, T.T., Tran, V.K., Pham, Q.H., Zenkour, A.M.: Extended four-unknown higher-order shear deformation nonlocal theory for bending, buckling and free vibration of functionally graded porous nanoshell resting on elastic foundation. Compos. Struct. **264**, 113737 (2021)
38. Huang, J., Momenzadeh, M., Lombardi, F.: An overview of nanoscale devices and circuits. IEEE Des. Test Comput. **24**, 304–311 (2007). https://doi.org/10.1109/MDT.2007.121
39. Lau, C.S., Mol, J.A., Warner, J.H., Briggs, G.A.D.: Nanoscale control of graphene electrodes. Phys. Chem. Chem. Phys. **16**, 20398–20401 (2014). https://doi.org/10.1039/c4cp03257h

40. Darban, H.: Size effect in ultrasensitive micro- and nanomechanical mass sensors. Mech. Syst. Signal Process. **200**, 110576 (2023). https://doi.org/10.1016/j.ymssp.2023.110576
41. Lassagne, B., Garcia-Sanchez, D., Aguasca, A., Bachtold, A.: Ultrasensitive mass sensing with a nanotube electromechanical resonator. Nano Lett. **8**, 3735–3738 (2008). https://doi.org/10.1021/NL801982V
42. Tao, Y., Wang, G., Zhu, J.: Nanorods and nanoblocks of polyaniline and their solvent resistance. Russ. J. Phys. Chem. A **90**, 183–186 (2016). https://doi.org/10.1134/S0036024416010349
43. Wang, X., Li, X.Q., Liu, T.Q., Zhao, L.D., Song, K.D., Ge, D.: Molecular dynamics simulation of interaction between nanorod and phospholipid molecules bilayer. Chin. Phys. B (2023). https://doi.org/10.1088/1674-1056/ac6ed8
44. Yang, W., Zhu, R., Zong, X.: ZnO nanowire-based corona discharge devices operated under hundreds of volts. Nanoscale Res. Lett. **11**(1), 90 (2016). https://doi.org/10.1186/S11671-015-1217-4
45. Krahne, R., Manna, L., Morello, G., Figuerola, A., George, C., Deka, S.: Catalytic Properties of Nanorods. Elsevier, Berlin, Heidelberg (2013)
46. Aydogdu, M.: Axial vibration of the nanorods with the nonlocal continuum rod model. Physica E Low-Dimens. Syst. Nanostruct. **41**, 861–864 (2009). https://doi.org/10.1016/j.physe.2009.01.007
47. Aydogdu, M.: Axial vibration analysis of nanorods (carbon nanotubes) embedded in an elastic medium using nonlocal elasticity. Mech. Res. Commun. **43**, 34–40 (2012). https://doi.org/10.1016/j.mechrescom.2012.02.001
48. Nassef, A.S.E.: Variable cross section nanorod model for longitudinal vibration analysis of cracked nanorods. Mater. Today Commun. (2026). https://doi.org/10.1016/j.mtcomm.2025.114305
49. Taima, M.S., El-Sayed, T., Farghaly, S.H.: Longitudinal vibration analysis of a stepped nonlocal rod embedded in several elastic media. J. Vib. Eng. Technol. **10**, 1399–1412 (2022). https://doi.org/10.1007/s42417-022-00454-7
50. Nazemnezhad, R.: A semi-analytical nonlinear approach for size-dependent analysis of longitudinal vibration in terms of axially functionally graded nanorods. Mech. Adv. Compos. Struct. **11**, 453–466 (2024). https://doi.org/10.22075/macs.2024.31981.1565
51. Uzun, B., Kafkas, U., Deliktaş, B., Yaylı, M.Ö.: Size-dependent vibration of porous Bishop nanorod with arbitrary boundary conditions and nonlocal elasticity effects. J. Vib. Eng. Technol. **11**, 809–826 (2023). https://doi.org/10.1007/s42417-022-00610-z
52. Uzun, B.: Magnetic field and non-local effects on axial vibration of embedded nanorods reinforced with short fibers. Acta Mech. **236**, 4889–4920 (2025). https://doi.org/10.1007/s00707-025-04417-3
53. Arda, M., Majak, J., Mehrparvar, M.: Longitudinal wave propagation in axially graded Raylegh–Bishop nanorods. Mech. Compos. Mater. **59**, 1109–1128 (2024). https://doi.org/10.1007/s11029-023-10160-4
54. Xu, D., Lu, J., Zhang, K., Li, P., Sun, L.: Longitudinal vibration characteristics analysis of nonlocal rod structure with arbitrary internal elastic supports. J. Vib. Control **29**, 3893–3906 (2023). https://doi.org/10.1177/10775463221106534
55. Yazıcıoğlu, A., Civalek, Ö.: Free axial and torsional vibration of boron nitride nanorods using nonlocal finite element method. J. Comput. Appl. Mech. **57**, 107–121 (2026). https://doi.org/10.22059/jcamech.2025.403575.1634
56. Numanoğlu, H.M., Akgöz, B., Civalek, Ö.: On dynamic analysis of nanorods. Int. J. Eng. Sci. **130**, 33–50 (2018). https://doi.org/10.1016/j.ijengsci.2018.05.001
57. Maugin, G.A.: Viscoelasticity of solids (Old and new). Solid Mech. Appl. **223**, 157–176 (2016). https://doi.org/10.1007/978-3-319-26593-3_7
58. Rahmani, A., Safaei, B., Qin, Z.: On wave propagation of rotating viscoelastic nanobeams with temperature effects by using modified couple stress-based nonlocal Eringen's theory. Eng. Comput. **38**, 2681–2701 (2022). https://doi.org/10.1007/s00366-021-01429-0
59. Alrubea, N.A., Abouelregal, A.E.: Thermoelastic dynamics of viscoelastic nanobeams on elastic foundations under multi-physics interactions. Results Eng. (2025). https://doi.org/10.1016/j.rineng.2025.106154
60. Balci, M.N.: Axial forced vibration problem for a viscoelastic nanorod involving radially graded porosity. J. Braz. Soc. Mech. Sci. Eng. **47**, 203 (2025). https://doi.org/10.1007/s40430-025-05497-x
61. Kadioglu, H.G., Yayli, M.O.: Axial vibration of a viscoelastic FG nanobeam with arbitrary boundary conditions. J. Vib. Eng. Technol. **13**, 96 (2025). https://doi.org/10.1007/s42417-024-01671-y
62. Kadıoğlu, H.G., Uzun, B., Civalek, Ö., Yaylı, M.Ö.: Dynamic behavior of micromorphic viscoelastic Euler–Bernoulli beams under viscoelastic boundary constraints. Acta Mech. **236**, 4475–4490 (2025). https://doi.org/10.1007/s00707-025-04364-z
63. Mohamed, N.A., Shanab, R.A., Eltaher, M.A., Abdelrahman, A.A.: Vibration response of viscoelastic perforated higher-order nanobeams rested on an elastic substrate under moving load. Acta Mech. **235**, 1213–1233 (2024). https://doi.org/10.1007/s00707-023-03776-z
64. Shakhlavi, S.J.: Nonlinear nonlocal damping effects under magnetic loads of a ferromagnetic-viscoelastic nanotube exposed to a nonlinear elastic medium with nonlocal viscosity. Commun. Nonlinear Sci. Numer. Simul. **130**, 107690 (2024). https://doi.org/10.1016/j.cnsns.2023.107690
65. Abouelregal, A.E., Sedighi, H.M.: Magneto-thermoelastic behaviour of a finite viscoelastic rotating rod by incorporating Eringen's theory and heat equation including Caputo–Fabrizio fractional derivative. Eng. Comput. **39**, 655–668 (2023). https://doi.org/10.1007/s00366-022-01645-2
66. Gul, U., Aydogdu, M.: On the axial vibration of viscously damped short-fiber-reinforced nano/micro-composite rods. J. Vib. Eng. Technol. **11**(3), 1327–1341 (2022). https://doi.org/10.1007/s42417-022-00643-4
67. Youssef, H.M., Alharbi, N.H.: The vibration of a nanobeam under generalized thermoviscoelasticity theory based on thermomass motion subjected to ramp-type heat. Mech. Time-Depend. Mater. **28**, 1421–1440 (2024). https://doi.org/10.1007/s11043-023-09625-9
68. Abouelregal, A.E., Megahid, S.F., Atta, D., Al-Azmi, A.M.K.: Thermoelectric interactions in Euler–Bernoulli microbeams under the influence of a thermal pulse via the size-dependent couple stress model. Mech. Time-Depend. Mater. **28**, 2619–2641 (2024). https://doi.org/10.1007/s11043-023-09661-5
69. Shi, X., Ma, Y.: Memory effect analysis of magneto-thermoelastic response of viscoelastic rotating nanobeams based on nonlocal and modified coupled stress elasticity theories. Mech. Time-Depend. Mater. **29**, 18 (2025). https://doi.org/10.1007/s11043-024-09757-6

70. Moradi, A., Ghanbarzadeh, A., Shishesaz, M., Sedighi, H.M.: Vibrational characteristics and critical damping behavior of nonlocal lipid/graphene sandwich nanoplates by incorporating viscoelastic features. Mech. Time-Depend. Mater. **29**, 21 (2025). https://doi.org/10.1007/s11043-024-09751-y
71. Su, X., Xie, L., Wu, Y., Xu, W.: Effective viscoelastic properties of particle-reinforced composites with inhomogeneous interphases, irregularly shaped and non-uniformly sized particles: a micromechanical model. Eur. J. Mech. A. Solids **116**, 105929 (2026). https://doi.org/10.1016/j.euromechsol.2025.105929
72. Dastgir, N., Ansari, R., Hassanzadeh-Aghdam, M.K., Jamali, J., Sahmani, S.: A unified Mori-Tanaka/finite element approach for investigating piezoelectric ellipsoidal particle-reinforced composite energy harvesters with various configurations. Eur. J. Mech. A. Solids **116**, 105921 (2026). https://doi.org/10.1016/j.euromechsol.2025.105921
73. Mori, T., Tanaka, K.: Average stress in matrix and average elastic energy of materials with misfitting inclusions. Acta Metall. **21**, 571–574 (1973). https://doi.org/10.1016/0001-6160(73)90064-3
74. Zhao, S., Zhao, Z., Yang, Z., Ke, L.L., Kitipornchai, S., Yang, J.: Functionally graded graphene reinforced composite structures: a review. Eng. Struct. **210**, 110339 (2020). https://doi.org/10.1016/J.ENGSTRUCT.2020.110339
75. Kuo, M.C., Tsai, C.M., Huang, J.C., Chen, M.: PEEK composites reinforced by nano-sized SiO2 and A1 2O3ˆOs particulates. Mater. Chem. Phys. **90**, 185–195 (2005). https://doi.org/10.1016/j.matchemphys.2004.10.009
76. Serra-Aguila, A., Puigoriol-Forcada, J.M., Reyes, G., Menacho, J.: Viscoelastic models revisited: characteristics and interconversion formulas for generalized Kelvin–Voigt and Maxwell models. Acta Mech. Sin. **35**, 1191–1209 (2019). https://doi.org/10.1007/s10409-019-00895-6

Publisher's Note Springer Nature remains neutral with regard to jurisdictional claims in published maps and institutional affiliations.